Kinematic Model Based Sensor Fusion for Inertial Measurement Units in Injury Biomechanics

Undergraduate Honors Thesis

By

Noah Izaac Eckstein

The Ohio State University

2021

Thesis Committee

Dr. Yun-Seok Kang, Advisor

Dr. Manoj Srinivasan, Committee Member

Abstract

Accurate kinematic measurement of human body segments is central to many investigations in biomechanics. The use of Inertial Measurement Units (IMUs) for this purpose is becoming increasingly effective in low acceleration regimes in part due to the incorporation of human body kinematic models in the sensor fusion process. For impact scenarios in injury biomechanics, the required sample rates and measuring ranges are larger than those of current commercial IMU systems with human model based fusion algorithms. Without sophisticated fusion algorithms that interface with impact-rated IMUs, injury biomechanics research has to rely on camera-based motion capture systems to ensure reliable measurements of body segment position and orientation (i.e., pose). The objective of this research is to develop a novel model based sensor fusion algorithm for impact-rated IMUs to reduce the necessity of camera-based pose measurements in injury biomechanics experiments. The scope of the present study focuses on state estimation for anthropomorphic test device (ATD) upper limbs, but the methodology can be intuitively extended to the entire body. The algorithm takes in acceleration, angular velocity, and angular acceleration measurements from IMUs mounted to the ATD and outputs piecewise polynomial estimates for the joint angles between ATD segments, as well as the six degrees of freedom of the ATD thoracic spine with respect to the inertial reference frame. These polynomials can be differentiated analytically to evaluate the full kinematic state of the ATD upper limb/thoracic spine assembly. The algorithm uses offline optimization for maximum likelihood estimation, relying on a zero mean gaussian

noise model for the measurements and a kinematic model for the ATD upper limb/thoracic spine to evaluate the likelihood of a given set of polynomial estimates. For simulated measurements augmented with gaussian noise based on the sensor uncertainties, the algorithm was promising. Due to restrictions on sensor availability, experimental validation of the algorithm was postponed, but future work will use physical experiments to compare the algorithm pose estimates to measurements from a camera-based motion capture system.

Table of Contents

Abstract ii
List of Tables vi
List of Figures vii
Chapter 1. Introduction 9
1.1. Injury Biomechanics Context 9
1.2. Pose Estimation from IMU Measurements 11
1.3. Focus of Thesis 13
Chapter 2. Methodology 14
2.1. Overview of Method 14
2.2. IMU placement 15
2.3. Kinematic Model 18
2.4. Piecewise Polynomial Breakpoint Selection 26
2.5. Finding the Maximum Likelihood Polynomial Approximation 30
2.5.1. Generating the Initial Seed 34
2.6. Evaluation in Simulation 37
Chapter 3. Results 39
3.1. Breakpoint Selection 39
3.2. Comparison of Overall Performance to Dead Reckoning 45
3.2.1. Example Plots from Pulse 1 45
3.2.2. Performance Across all Trials 58
Chapter 4. Discussion 65
4.1. Instrumentation Scheme 65
4.2. Polynomials 66
4.3. Theoretical Limitations 68
4.4. Study limitations 69

4.5. Applicability to PMHS Testing 73
Chapter 5. Summary and Conclusions 74
5.1. Summary 74
5.2. Conclusions and Future work 76
Bibliography 78

List of Tables

Table 1. State Definitions 17
Table 2. Root Mean Squared Error for Each Pulse Individually 63
Table 3. Root Mean Squared Error Across All Pulses..... 64

List of Figures

Figure 1. Link Names and Sensor Types 15
Figure 2. Joint Axes and Sensor Names 16
Figure 3. Exemplar First Breakpoint Selection Iteration 40
Figure 4. Exemplar Second Breakpoint Selection Iteration 41
Figure 5. Exemplar Third Breakpoint Selection Iteration 42
Figure 6. Exemplar Fourth Breakpoint Selection Iteration 43
Figure 7. Exemplar Final Breakpoint Selection Iteration 44
Figure 8. φ Estimates, Pulse 1 46
Figure 9. θ Estimates, Pulse 1 47
Figure 10. σ Estimates, Pulse 1 48
Figure 11. x Estimates, Pulse 1 49
Figure 12. y Estimates, Pulse 1 50
Figure 13. z Estimates, Pulse 1 51
Figure 14. s Estimates, Pulse 1 52
Figure 15. ρ Estimates, Pulse 1 53
Figure 16. f Estimates, Pulse 1 54
Figure 17. β Estimates, Pulse 1 55
Figure 18. L Estimates, Pulse 1 56
Figure 19. ϵ Estimates, Pulse 1 57
Figure 20. Root Mean Squared Error for Pulse 1 Relative Pose Estimates 59
Figure 21. Root Mean Squared Error for Pulse 2 Relative Pose Estimates 60
Figure 22. Root Mean Squared Error for Pulse 3 Relative Pose Estimates 61

Chapter 1. Introduction

1.1. Injury Biomechanics Context

The field of injury biomechanics is characterized by the study of the human body response to potentially injurious external events. A common general methodology employed in injury biomechanics experiments is to expose a postmortem human subject (PMHS) to a potentially injurious event, such as an impact, and measure the kinematic and kinetic response of the body segments of specific interest. These biomechanical data can be correlated to the occurrence of injury, and these correlations inform the development of injury criteria and injury risk curves, which describe the human tolerance to injury in terms of quantitative measurements [1]. These injury criteria and risk curves can be scaled to enable evaluation of the likelihood of injury in tests which use anthropomorphic test devices (ATDs) (i.e., crash test dummies), as an ATD does not actually exhibit injuries, but its kinematic and kinetic response can be measured. While no injury criteria currently identified directly depend on whole body kinematic measurements [1], it is necessary that the whole body kinematic response of ATDs closely match that of humans. An example of this importance can be seen in frontal automotive crash simulations, where the whole body kinematic response dictates the abdominal and thoracic interaction with restraint systems [2]. In high energy test

environments, the standard for whole body position and orientation measurement of both ATDs and PMHSs has been optoelectronic stereophotogrammetric systems (OSSs) which utilize reflective markers and multiple camera vantage points to construct a three-dimensional (3D) measurement of position for each marker [3]. By outfitting each body segment with at least three markers, the marker positions can be used to evaluate both position and orientation of each segment through time. However, these systems suffer from issues with extensive setup and calibration requirements, and for full accuracy, each marker must always be in view of multiple cameras [3], which is detrimental in highly dynamic environments where markers are likely to be occluded or even ejected. As well, OSSs lack the ability to estimate the derivatives of position and orientation without noise amplifying numerical differentiation. Moreover, the most common kinematic measurements used in injury criteria are linear and angular accelerations, thus necessitating excessively noisy double numerical differentiation of OSS measurements if they are to be used to evaluate injury criteria. As a result, OSS measurements are used only as position and orientation references, while inertial sensors, such as angular velocity sensors and linear accelerometers, are used to directly measure the derivatives. Compact inertial measurement units (IMUs) equipped with sensor arrays that can measure 3D angular velocity, 3D linear specific force, and sometimes 3D angular acceleration are used in injury biomechanics for this purpose [4]. Given the difficulties associated with OSSs and the necessary use of IMUs alongside them for PMHS and ATD testing, a natural question emerges as to the viability of IMUs in position and orientation estimation. If whole body position and orientation estimates of comparable quality to

those of OSSs can be achieved from IMU measurements alone, then the use of OSSs in impact experiments in injury biomechanics may be unnecessary.

1.2. Pose Estimation from IMU Measurements

The most basic and intuitive approach to estimating pose (i.e., position and orientation) from a single IMU with 3D ARS and 3D accelerometers is based only on numerical integration. First, the ARS data is converted to a form which represents the time derivative of the chosen parametrization for orientation. In this form, they are numerically integrated to achieve estimates for the senor orientation in the inertial reference frame. Next, the orientation estimates are used to transform the accelerometer data from the local, sensor fixed reference frame into the inertial reference frame. Because linear accelerometers directly measure specific force, the local acceleration due to gravity must be added to the transformed accelerometer data to correct for the absence of free fall acceleration in the accelerometer readings. This yields an estimate for the sensor's coordinate acceleration with respect to the inertial frame. The coordinate acceleration is then numerically integrated to achieve estimates of sensor velocity and position in the inertial reference frame. This method, commonly referred to as dead reckoning, naturally suffers from problems with numerical integration drift [5]. Drift introduced during numerical integration of the angular velocity is compounded in the double integration of the kinematic acceleration estimates, as drift in the numerically integrated orientation estimates results in imperfect correction for gravity due to imperfect transformation into the inertial reference frame. In general, the only way to address drift in IMU pose estimates is to utilize directly observable (i.e., not numerically

integrated) information about pose in the estimation process. For a single IMU, this additional information must come from a reference with known position or orientation in the inertial frame. Often, this reference is obtained by incorporating 3D magnetometers into the IMU [5]. The magnetometer acts as a compass, providing information about the sensor heading in the inertial reference frame. In environments where the magnetic field in the vicinity of the IMU is not rigidly attached to the inertial frame, as is often the case when ferromagnetic materials and/or electronic components make up the object being measured, or in cases where the magnetic field is non-homogeneous throughout the inertial reference frame, as is common in indoor environments, the use of magnetometers is problematic [5].

In applications where estimates of pose for a kinematic chain of objects is desired, the additional information required to mitigate drift can be obtained simply by considering the kinematic constraints of the system of interest, without the use of magnetometers. This has been done using knowledge of the degrees of freedom and/or range of motion of the joints between segments to construct constraints on the angular velocities or orientations of links in the chain [6-13], and it has also been done by simply constraining the ends of the links to remain coincident at shared joint centers [14-20]. Most of these techniques require IMUs on every segment in the chain, however, alternating IMU placements, where every other link is left without a sensor, have been used with success [21]. These methods require the use of either Kalman filter type techniques or optimization to incorporate the kinematic constraints. For a more in depth discussion of the aforementioned techniques, refer to [22].

Naturally, these techniques are applicable to human pose estimation, as the human body is subject to kinematic constraints. In turn, kinematic constraints have been used to reduce drift in pose estimation with great success within biomechanics. However, the only available examples in the literature have considered relatively low acceleration regimes (e.g., gait analysis, rehabilitation, athletics, etc.). To my knowledge, the value of kinematic model based sensor fusion for high acceleration regimes, such as those common within injury biomechanics, has not been explored.

1.3. Focus of Thesis

The objective of this research was to develop and validate a kinematic model based sensor fusion algorithm for implementation with impact IMUs to reduce the necessity of camera-based pose measurements in injury biomechanics experiments. Only the ATD upper limb and thoracic spine pose was considered, but the intent was to provide a first step toward incorporating kinematic models in the sensor fusion process for entire ATDs, and, eventually, entire PMHSs. Plans to compare the performance of the algorithm and instrumentation scheme developed herein with OSS measurements were left for future work due to scheduling difficulties related to global events. Thus, this thesis presents only simulation experiments.

Chapter 2. Methodology

2.1. Overview of Method

In this thesis, I developed a magnetometer free IMU placement scheme and corresponding sensor fusion algorithm that utilizes maximum likelihood estimation to produce estimates of the full kinematic state of an ATD upper limb and thoracic spine assembly during impact experiments. The instrumentation scheme employs a total of four impact rated IMUs, each capable of measuring 3D specific force and 3D angular velocity, one of which having the additional capability of measuring 3D angular acceleration. The sensor fusion algorithm generates continuous, twice differentiable piecewise polynomial estimates of all joint angles between ATD segments as well as the six degrees of freedom of the thoracic spine segment with respect to the inertial reference frame. These polynomials can be differentiated to define the full kinematic state of the ATD down to accelerations. The algorithm has three distinct steps: polynomial breakpoint selection, initial guess generation, and maximal likelihood estimation via a largescale interior point optimization method. The algorithm relies on a zero mean gaussian noise model for the sensor measurements and a rigid kinematic model for the ATD to evaluate the likelihood

of a given set of polynomial estimates, which then serves as the objective function for the optimization procedure. I tested the algorithm in simulation.

2.2. IMU placement

Figure 1 shows the placement of the IMUs on the ATD arm assembly and the names of the distinct links in the ATD arm kinematic chain. Figure 2 shows the joint axes and the sensor names. Table 1 provides information about the state variables, which consist of all joint angles and the six degrees of freedom of the thoracic spine with respect to the inertial reference frame.

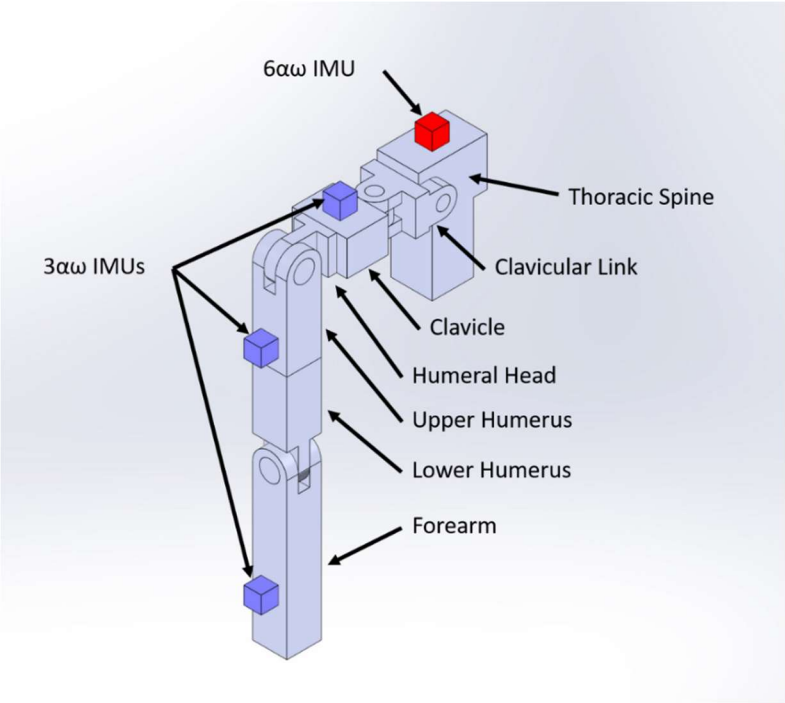

The IMUs labeled 3αω measure 3D angular velocity and specific force, and the IMU labeled 6αω has the additional ability to measure 3D angular acceleration.

Figure 1. Link Names and Sensor Types

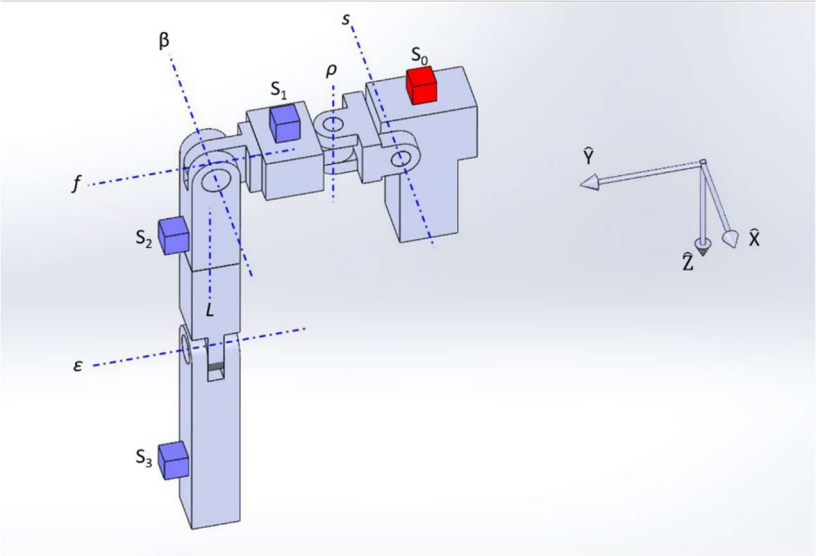

The linkage is shown when all angles are zero. In this configuration, all local body frames are aligned with the inertial reference frame, denoted by the coordinate system shown at the right. The sensor measurement frames are aligned with the local frame of the link to which they are attached. Positive angular displacements follow the right-hand rule, with the direction of the joint axes defined to point along the coordinate axes to which they are parallel when all angles are zero.

Figure 2. Joint Axes and Sensor Names

State	Description	Axis
φ	First Euler angle of the thoracic spine	$\hat{Z}$, inertial
θ	Second Euler angle of the thoracic spine	$\hat{Y}$, inertial
σ	Third Euler angle of the thoracic spine	$\hat{X}$, inertial
x	Position of thoracic spine measurement center	$\hat{X}$, inertial
y	Position of thoracic spine measurement center	$\hat{Y}$, inertial
z	Position of thoracic spine measurement center	$\hat{Z}$, inertial
s	Elevation/depression angle between the clavicular link and thoracic spine	$\hat{X}$, body
ρ	Protraction/retraction angle between clavicular link and clavicle	$\hat{Z}$, body
f	Flexion/extension angle of the shoulder, between clavicle and humeral head	$\hat{Y}$, body
β	Abduction/adduction of the shoulder, between humeral head and upper humerus	$\hat{X}$, body
L	Mediolateral rotation angle of the shoulder, between upper and lower humeri	$\hat{Z}$, body
ϵ	Flexion/extension of the elbow, between lower humerus and forearm	$\hat{Y}$, body

Table 1. State Definitions

This placement uses the fewest possible IMUs while still ensuring that, no matter the values of the joint angles, all joint angles can be approximated from estimates of the sensor orientations with respect to a common frame. This is because 1) the sensors are placed on every other link, which places two joint angles between each sensor, and 2) for all links with two joint axes passing through them, those two joint axes are rigidly fixed to remain orthogonal to one another. It is therefore guaranteed that the true relative rotation matrix from one sensor frame to the next will always be decomposable into two distinct rotations about the joint axes between the sensors. This is important to ensure that an initial seed for the optimization procedure can always be generated from numerical integration of the angular velocity measurements. I will discuss this further in Chapter 2.5.

In the analysis of the kinematic chain, it is necessary to assign one of the links as the base link from which all other link kinematics are referenced. Because the base link

pose defines the overall pose of the ATD in the inertial reference frame, I decided this link should be given extra sensing capability, hence the inclusion of a single 6αω IMU. I assigned the base link role to the thoracic spine because, in an actual ATD, the thoracic spine typically has the most available space for mounting of additional sensors, making it the best candidate for placement of the 6αω IMU, which requires room than the 3αω IMUs. Additionally, because the thoracic spine is the most central link in the ATD upper body assembly (assuming it has both arms), estimating the global orientation by tracking the thoracic spine's global orientation reduces the effect of global orientation error on global position error for the distal ends of the ATD.

2.3. Kinematic Model

To construct the kinematic model, I assumed the links of the ATD are rigid, and each joint is a single degree of freedom revolute joint. With these assumptions, the ATD arm can be reduced to a simple kinematic chain, with the kinematic state of any link, as defined with respect to the basis vectors of its body fixed frame, being entirely a function of the kinematics of the previous link in the chain and the kinematics of the joint between them. For two links, *i* and *j*, separated by a single degree of freedom revolute joint with scalar angular displacement λ in radians about a unit vector $\hat{w}_\lambda$ rigidly fixed to both links, the angular velocity ($\vec{\omega}, rad/s$), angular acceleration ($\vec{\alpha}, rad/s^2$), and linear specific force ($\vec{a}, m/s^2$) of link *j* in its body fixed frame can be written in terms of link *i* kinematics as shown in Equations 1-3. For convenience, I assign the origin of the body fixed coordinate system of segment *i* to be coincident with the joint center between *i* and

j. Likewise, coordinate system *j* originates from the joint center that would connect it with the next segment in the chain (if there were one).

$$\overrightarrow{\omega_j} = {R_{ij}}^T \overrightarrow{\omega_i} + \dot{\lambda}\hat{w}_\lambda \qquad (1)$$

$$\overrightarrow{\alpha_j} = {R_{ij}}^T\left(\overrightarrow{\alpha_i} + \overrightarrow{\omega_i} \times \dot{\lambda}\hat{w}_\lambda\right) + \ddot{\lambda}\hat{w}_\lambda \qquad (2)$$

$$\overrightarrow{a_j} = {R_{ij}}^T \overrightarrow{a_i} + \overrightarrow{\omega_j} \times \left(\overrightarrow{\omega_j} \times \overrightarrow{r_j}\right) + \overrightarrow{\alpha_j} \times \overrightarrow{r_j} \qquad (3)$$

Where:

for $\lambda = 0$, coordinate systems i and j are aligned

$\overrightarrow{\omega_j}$, $\overrightarrow{\alpha_j}$, $\overrightarrow{a_j}$= angular velocity, angular acceleration, specific force, respectively, experienced at the origin of frame j expressed in frame j

R_{ij} = rotation matrix, rotates vectors λ radians about the $\hat{w}_\lambda$ in the input space; transforms vectors from frame j to frame i

$\dot{\lambda}$, $\ddot{\lambda}$ = first and second derivatives of λ with respect to time, respectively

$\overrightarrow{r_j}$ = position vector from origin i to origin j expressed in frame j

$\hat{w}_\lambda$ expressed in either frame i or j (same coordinates in both frames).

Note that Equation 3 only applies for calculating the specific force at the origin of the *j* coordinate system. To calculate specific forces at different locations on link *j* (e.g., measurement centers) $\overrightarrow{r_j}$ must be replaced with a vector that goes from origin *i* to the point of interest. As well, note that $\hat{w}_\lambda$ is invariant under the transformation ${R_{ij}}^T$ and that, for any two vectors $\vec{A}$ and $\vec{B}$ in $\mathbb{R}^3$, $\vec{A} \times \vec{B} = (\vec{A} + c\vec{B}) \times \vec{B}$, where *c* is any arbitrary scalar. Therefore, $\vec{\alpha}_j$ may be rewritten in terms of $\vec{\omega}_j$ as shown in Equation 2.1.

$$\overrightarrow{\alpha_j} = {R_{ij}}^T \overrightarrow{\alpha_i} + \overrightarrow{\omega_j} \times \dot{\lambda}\hat{w}_\lambda + \ddot{\lambda}\hat{w}_\lambda \qquad (2.1)$$

Equations 1-3 can be used to generate kinematic equations for every link in the ATD kinematic chain except for the thoracic spine, which I consider the base link in my analysis. For the base link, I chose to parameterize the kinematic equations in terms of Euler angles, as they are simple to implement in an optimization procedure because they require only three parameters and no orthogonality or magnitude constraints (as in the cases of rotation matrices or quaternions). As well, in most ATD testing, vehicle constraint systems prevent the thorax from rotating 90 degrees about any axis, thus mitigating the practical detriment associated with the possibility of gimbal lock. Using a 3-2-1 Euler angle convention (chosen arbitrarily), the angular velocity ($\vec{\omega}_0, rad/s$), angular acceleration ($\vec{\alpha}_0, rad/s^2$), and linear specific force ($\vec{a}_0, m/s^2$) of the thoracic spine in its body fixed frame can be written in terms of Euler angles φ, θ, σ (3,2,1, respectively) and x, y, z positions in the inertial frame as shown in Equations 4 – 6 (refer to Figure 2 for more information about these states). Equations 4 and 5 follow from Equations 1-3, while Equation 6 follows from the definition of 3-2-1 Euler angles. The origin of the thoracic spine coordinate system is taken to be the measurement center of the S_0.

$$\vec{\omega}_0 = R_z(-\varphi)\left(R_y(-\theta)\begin{bmatrix}\dot{\sigma}\\0\\0\end{bmatrix} + \begin{bmatrix}0\\\dot{\theta}\\0\end{bmatrix}\right) + \begin{bmatrix}0\\0\\\dot{\varphi}\end{bmatrix} \qquad (4)$$

$$\vec{\alpha}_0 = R_z(-\varphi)\left(\left(R_y(-\theta)\begin{bmatrix}\dot{\sigma}\\0\\0\end{bmatrix} + \begin{bmatrix}0\\\dot{\theta}\\0\end{bmatrix}\right) \times \begin{bmatrix}0\\0\\\dot{\varphi}\end{bmatrix} + R_y(-\theta)\begin{bmatrix}\ddot{\sigma}\\0\\\dot{\sigma}\dot{\theta}\end{bmatrix} + \begin{bmatrix}0\\\ddot{\theta}\\0\end{bmatrix}\right) + \begin{bmatrix}0\\0\\\ddot{\varphi}\end{bmatrix} \qquad (5)$$

$$\vec{a}_0 = R_z(-\varphi)R_y(-\theta)R_x(-\sigma)\begin{bmatrix} \ddot{x} \\ \ddot{y} \\ \ddot{z} - g \end{bmatrix} \qquad (6)$$

Where:

$R_x(\lambda)$ = rotation matrix, rotates vectors λ radians about the x axis of the input space

$R_y(\lambda)$ = rotation matrix, rotates vectors λ radians about the y axis of the input space

$R_z(\lambda)$ = rotation matrix, rotates vectors λ radians about the z axis of the input space

g = magnitude of gravitational acceleration.

Using Equations 1-6, I developed a set of kinematic equations that can be used to calculate estimates for the measurable kinematics experienced by all the sensors based on estimates of the ATD states and their first two derivatives. The Equations pertaining to the measurements of S_0 are already listed in Equations 4-6. Equations 7-13 can be used to estimate the measurements for S_1. Equations 7-10 estimate the kinematics of the clavicular link, which are required to use Equations 11-13 to estimate the measurements of S_1. Because S_1 is a 3αω IMU, only Equations 11 and 13 correspond to measurements.

$$\vec{a}_{0j} = \vec{a}_0 + \vec{\omega}_0 \times (\vec{\omega}_0 \times \vec{r}_0) + \vec{\alpha}_0 \times \vec{r}_0 \qquad (7)$$

$$\vec{\omega}_{cl} = R_x(-s)\vec{\omega}_0 + \begin{bmatrix} \dot{s} \\ 0 \\ 0 \end{bmatrix} \qquad (8)$$

$$\vec{\alpha}_{cl} = R_x(-s)\vec{\alpha}_0 + \vec{\omega}_{cl} \times \begin{bmatrix} \dot{s} \\ 0 \\ 0 \end{bmatrix} + \begin{bmatrix} \ddot{s} \\ 0 \\ 0 \end{bmatrix} \qquad (9)$$

$$\vec{a}_{clj} = R_x(-s)\vec{a}_{0j} + \vec{\omega}_{cl} \times (\vec{\omega}_{cl} \times \vec{r}_{cl}) + \vec{\alpha}_{cl} \times \vec{r}_{cl} \qquad (10)$$

$$\vec{\omega}_1 = R_z(-\rho)\vec{\omega}_{cl} + \begin{bmatrix} 0 \\ 0 \\ \dot{\rho} \end{bmatrix} \qquad (11)$$

$$\vec{\alpha}_1 = R_z(-\rho)\vec{\alpha}_{cl} + \vec{\omega}_1 \times \begin{bmatrix} 0 \\ 0 \\ \dot{\rho} \end{bmatrix} + \begin{bmatrix} 0 \\ 0 \\ \ddot{\rho} \end{bmatrix} \qquad (12)$$

$$\vec{a}_1 = R_z(-\rho)\vec{a}_{clj} + \vec{\omega}_1 \times (\vec{\omega}_1 \times \vec{m}_1) + \vec{\alpha}_1 \times \vec{m}_1 \qquad (13)$$

Where:

$\vec{a}_{0j}$ = specific force experienced at the center of joint s expressed in the thoracic spine frame

$\vec{r}_0$ = position vector from the measurement center of S_0 to the center of joint s expressed in the thoracic spine frame

$\vec{\omega}_{cl}$ = angular velocity of the clavicular link expressed in its local frame

$\vec{\alpha}_{cl}$ = angular acceleration of the clavicular link expressed in its local frame

$\vec{a}_{clj}$ = specific force experienced at the center of joint ρ expressed in the clavicular link frame

$\vec{r}_{cl}$ = position vector from the center of joint s to the center of joint ρ expressed in the clavicular link frame

$\vec{\omega}_1, \vec{\alpha}_1, \vec{a}_1$ = angular velocity, angular acceleration, specific force, respectively; experienced by S_1 and expressed in its local frame (i.e., the clavicle frame).

$\vec{m}_1$ = position vector from the center of joint ρ to the measurement center of S_1 expressed in its local frame.

Just as Equations 7-13 calculate estimates for the measurements of S_1 in its local frame based on the estimates for the measurements of S_0 and the kinematics of the *s* and ρ joints, Equations 14-20 calculate estimates for the measurements of S_2 in its local frame based on the estimates for the measurements of S_1 and the kinematics of the f and β joints.

$$\vec{a}_{1j} = \vec{a}_1 + \vec{\omega}_1 \times \left(\vec{\omega}_1 \times (\vec{r}_1 - \vec{m}_1)\right) + \vec{\alpha}_1 \times (\vec{r}_1 - \vec{m}_1) \qquad (14)$$

$$\vec{\omega}_{hh} = R_y(-f)\vec{\omega}_1 + \begin{bmatrix} 0 \\ \dot{f} \\ 0 \end{bmatrix} \qquad (15)$$

$$\vec{\alpha}_{hh} = R_y(-f)\vec{\alpha}_1 + \vec{\omega}_{hh} \times \begin{bmatrix} 0 \\ \dot{f} \\ 0 \end{bmatrix} + \begin{bmatrix} 0 \\ \ddot{f} \\ 0 \end{bmatrix} \qquad (16)$$

$$\vec{a}_{hh} = R_y(-f)\vec{a}_{1j} + \vec{\omega}_{hh} \times (\vec{\omega}_{hh} \times \vec{r}_{hh}) + \vec{\alpha}_{hh} \times \vec{r}_{hh} \qquad (17)$$

$$\vec{\omega}_2 = R_x(-\beta)\vec{\omega}_{hh} + \begin{bmatrix} \dot{\beta} \\ 0 \\ 0 \end{bmatrix} \qquad (18)$$

$$\vec{\alpha}_2 = R_x(-\beta)\vec{\alpha}_{hh} + \vec{\omega}_2 \times \begin{bmatrix} \dot{\beta} \\ 0 \\ 0 \end{bmatrix} + \begin{bmatrix} \ddot{\beta} \\ 0 \\ 0 \end{bmatrix} \qquad (19)$$

$$\vec{a}_2 = R_x(-\beta)\vec{a}_{hhj} + \vec{\omega}_2 \times (\vec{\omega}_2 \times \vec{m}_2) + \vec{\alpha}_2 \times \vec{m}_2 \qquad (20)$$

Where:

$\vec{a}_{1j}$ = specific force experienced at the center of joint f expressed in the clavicle frame

$\vec{r}_1$ = position vector from the center of joint ρ to the center of joint f expressed in the clavicle frame

$\vec{\omega}_{hh}$ = angular velocity of the humeral head expressed in its local frame

$\vec{\alpha}_{hh}$ = angular acceleration of the humeral head expressed in its local frame

$\vec{a}_{hhj}$ = specific force experienced at the center of joint β expressed in the humeral head frame

$\vec{r}_{hh}$ = position vector from the center of joint f to the center of joint β expressed in the humeral head frame

$\vec{\omega}_2, \vec{\alpha}_2, \vec{a}_2$ = angular velocity, angular acceleration, and specific force, respectively; experienced by S_2, expressed in its local frame (i.e., the upper humerus frame)

$\vec{m}_2$ = position vector from the center of joint β to the measurement center of S_2 expressed in its local frame.

Finally, Equations 21-27 calculate estimates for the measurements of S_3 in its local frame based on the estimates for the measurements of S_2 and the kinematics of the L and ϵ joints.

$$\vec{a}_{2j} = \vec{a}_2 + \vec{\omega}_2 \times \left(\vec{\omega}_2 \times (\vec{r}_2 - \vec{m}_2)\right) + \vec{\alpha}_2 \times (\vec{r}_2 - \vec{m}_2) \qquad (21)$$

$$\vec{\omega}_{lh} = R_z(-L)\vec{\omega}_2 + \begin{bmatrix} 0 \\ 0 \\ \dot{L} \end{bmatrix} \qquad (22)$$

$$\vec{\alpha}_{lh} = R_z(-L)\vec{\alpha}_2 + \vec{\omega}_{lh} \times \begin{bmatrix} 0 \\ 0 \\ \dot{L} \end{bmatrix} + \begin{bmatrix} 0 \\ 0 \\ \ddot{L} \end{bmatrix} \qquad (23)$$

$$\vec{a}_{lhj} = R_z(-L)\vec{a}_{2j} + \vec{\omega}_{lh} \times (\vec{\omega}_{lh} \times \vec{r}_{lh}) + \vec{\alpha}_{lh} \times \vec{r}_{lh} \qquad (24)$$

$$\vec{\omega}_3 = R_y(-\epsilon)\vec{\omega}_{lh} + \begin{bmatrix} 0 \\ \dot{\epsilon} \\ 0 \end{bmatrix} \qquad (25)$$

$$\vec{\alpha}_3 = R_y(-\epsilon)\vec{\alpha}_{lh} + \vec{\omega}_3 \times \begin{bmatrix} 0 \\ \dot{\epsilon} \\ 0 \end{bmatrix} + \begin{bmatrix} 0 \\ \ddot{\epsilon} \\ 0 \end{bmatrix} \qquad (26)$$

$$\vec{a}_3 = R_y(-\epsilon)\vec{a}_{lhj} + \vec{\omega}_3 \times (\vec{\omega}_3 \times \vec{m}_3) + \vec{\alpha}_3 \times \vec{m}_3 \qquad (27)$$

Where:

$\vec{a}_{2j}$ = specific force experienced at the center of joint L expressed in the upper humerus frame

$\vec{r}_2$ = position vector from the center of joint β to the center of joint L expressed in the upper humerus frame

$\vec{\omega}_{lh}$ = angular velocity of the lower humerus expressed in its local frame

$\vec{\alpha}_{lh}$ = angular acceleration of the lower humerus expressed in its local frame

$\vec{a}_{hhj}$ = specific force experienced at the center of joint ϵ expressed in the lower humerus frame

$\vec{r}_{lh}$ = position vector from the center of joint L to the center of joint ϵ expressed in the lower humerus frame

$\vec{\omega}_3$, $\vec{\alpha}_3$, $\vec{a}_3$ = angular velocity, angular acceleration, and specific force, respectively; experienced by S_3, expressed in its local frame (i.e., the forearm frame)

$\vec{m}_3$ = position vector from the center of joint ϵ to the measurement center of S_3 expressed in its local frame.

Assuming the local measurement frames of the sensors are aligned with the local frames of their corresponding links, Equations 4-6, 11,13,18,20,25, and 27 directly correspond to the inertial measurements captured by the sensors. With the ability to calculate what the sensor measurements would be based on estimates of the degrees of freedom of the system and their time derivatives, it is then possible to construct the cost function for the optimization step, which I will describe in 2.5.

2.4. Piecewise Polynomial Breakpoint Selection

Due to the high sampling rates characteristic of impact testing, the data sets tend to be large. In the context of my algorithm, which utilizes offline optimization to estimate the degrees of freedom for the linkage, this is problematic. For some context, if the algorithm produced estimates for each state variable in the linkage at every time sample, an experiment sampled at 10 kHz and lasting only half a second would produce an optimization problem with 60,000 decision variables, and this is for only one arm. On top of the problem size, the algorithm would need to approximate the first two time derivatives of the states by way of numerical differentiation, which would introduce error in the procedure. To avoid these issues, I devised a functional approximation approach, where the states of the system are modeled as continuous, twice-differentiable piecewise polynomial functions of time. In this approach, the choice of the time locations for the break points between polynomials is important, as the break points must be placed so as to imbue the model with enough flexibility to capture the meaningful complexity of the data while limiting its flexibility enough to avoid overfitting and keep the number of decision variables low. One intuitive option for optimizing break point selection for a

given polynomial order and number of break points would be to allow the same optimization algorithm that optimizes the polynomial coefficients to also alter the break point locations as decision variables. However, this could only ever address the decisions of locating the break points in time; it could not address the decision as to how many break points, and therefor panels, should be used. Instead, I designed a break point selection procedure that runs before the optimization of the polynomial coefficients and passes these break points as invariable hyperparameters of the model.

For the model complexity of the individual panels in the piecewise polynomials, I chose 5^{th} order polynomials because they are the minimum order polynomial which allows the second derivatives to have time varying curvature between breakpoints. Largely, this was an arbitrary decision made on intuition. However, the method I devised for selecting the breakpoints works in principle for any polynomial order ≥ 3.

The break point selection method assumes that the excitation of the sensor measurements in time is a reasonable approximation of the excitation in the state variables in time. Therefore, it selects the break points based on the ability of the resulting piecewise polynomials to approximate the raw sensor measurements. It takes inputs of the sensor measurements, known variances for the noises of the sensors, and a prescribed polynomial order, O, which denotes the order of the polynomials intended to approximate the state variable positions. It functions by iteratively fitting piecewise polynomials of order $O - 2$ to the sensor measurements corresponding to accelerations (e.g. angular acceleration and specific force), adding new break points in every iteration based on the quality of fit within each panel. The fitting is executed via a quadratic

programming routine subject to linear equality constraints, where the objective function to be minimized is the sum of squared error for the fit, and the equality constraints correspond to continuity of the polynomials at break points (see Equation 36 in Chapter 2.5 for the structure of these constraints). The algorithm uses order $O-2$ polynomials because the high frequency behavior of the acceleration measurements is primarily a function of the second derivatives of the state variables, which will have order $O-2$ after differentiation. During a given iteration, the algorithm first fits piecewise polynomials with continuity constraints at the break points to the measurements from each sensor. Then, for each panel individually, it evaluates a weighted average of the squared error in the fit across all the different sensor measurements of interest, weighting the squared error for each individual sensor measurement by the inverse of the known noise variance for that sensor. For a panel in which all polynomials perfectly track the true value of their respective sensor measurements, this weighted average, which I will refer to as the weighted mean squared error (wMSE), would have an expected value of 1. Within panels with wMSE greater than a tuning constant c >1 (chosen to be 1.2), the algorithm inserts an additional break point according to Equations 28 and 29. Equations 28 and 30 together provide a mathematical definition for wMSE.

$$wSE_j = \sum_{i=1}^{m} \frac{\left(Y_{ij} - \hat{Y}_{ij}\right)^2}{Var_i} \qquad [28]$$

$$bp_{new} = \frac{\sum_{j=1}^{n} wSE_j t_j}{\sum_{j=1}^{n} wSE_j} \qquad [29]$$

$$wMSE = \frac{1}{mn} \sum_{j=1}^{n} wSE_j \qquad [30]$$

Where:

i = data channel index

j = time sample index; for the first time sample in the panel, j = 1

Var_i = known noise variance for data channel i;

Y_{ij} = sensor measurement from sensor i collected at time j

$\widehat{Y}_{ij}$ = polynomial estimate of Y_{ij}

m = number of data channels being used to select breakpoints

n = number of time samples in the panel.

Any panels containing fewer than $2(O-1)$ time samples (i.e, twice the number of time samples required to fully define a polynomial of order $O-2$) are ignored during the break point addition step, irrespective of their wMSE, to avoid producing degenerately small panels which lack the data required to keep the polynomial estimates stable. However, this does not guarantee that no such panels will be produced. Therefore, the final step of each iteration is another quadratic programing routine, this time subject to inequality constraints, where the decision variables are the locations of adjusted break points, the objective is the sum of squared differences between the adjusted break points and the set of break points previously identified by the algorithm, and the linear

inequality constraints are defined to ensure no panels may span fewer than $O-1$ time steps.

The algorithm starts in with no break points (i.e., the first iteration generates single polynomial estimates of order $O-2$ to approximate the full time series of data) and iterates until all panels either 1) have wMSE < c, or 2) span fewer than $2(O-1)$ time steps. In practice, I have never seen this routine produce panels that satisfy condition two without satisfying condition one as well.

I have no analytical bases on which to claim Equation 29 produces an optimal placement for the new break point. However, an intuitive explanation for why it is reasonable can be seen in the fact that the time location of the new breakpoint, bp_{new}, corresponds to the first moment of the presently unaccounted-for measurement variance within that panel. The two new panels created by the break will therefore be, in some sense, balanced. For the purposes of this research, it suffices to say that my break point selection method works well enough. I will show its sufficiency in Chapter 3.

2.5. Finding the Maximum Likelihood Polynomial Approximation

Once a reasonable set of break points is identified, the algorithm proceeds to the final step, which is to optimize a set of coefficients that comprise piecewise polynomial estimates of the states of the ATD thoracic spine and upper limb assembly (see table 1). This is done via a largescale interior point optimization procedure (fmincon, MathWorks, Natick, MA). The objective function for the optimization is stated below in Equation 31.

$$F(B, bp, \mu, \delta) = \sum_{j=1}^{n} \left(\frac{\left(\vec{\alpha}_0^j - \hat{\alpha}_0^j\right)^T \left(\vec{\alpha}_0^j - \hat{\alpha}_0^j\right)}{Var_\alpha} + \sum_{i=0}^{3} \left(\frac{\left(\vec{\omega}_i^j - \hat{\omega}_i^j\right)^T \left(\vec{\omega}_i^j - \hat{\omega}_i^j\right)}{Var_\omega} + \frac{\left(\vec{a}_i^j - \hat{a}_i^j\right)^T \left(\vec{a}_i^j - \hat{a}_i^j\right)}{Var_a} \right) \right) + \left(\begin{bmatrix} \hat{x} \\ \hat{y} \\ \hat{z} \end{bmatrix}^T \begin{bmatrix} \hat{x} \\ \hat{y} \\ \hat{z} \end{bmatrix} + \begin{bmatrix} \dot{\hat{x}} \\ \dot{\hat{y}} \\ \dot{\hat{z}} \end{bmatrix}^T \begin{bmatrix} \hat{x} \\ \hat{y} \\ \hat{z} \end{bmatrix} + \begin{bmatrix} \hat{\varphi} \\ \hat{\theta} \\ \hat{\sigma} \end{bmatrix}^T \begin{bmatrix} \hat{\varphi} \\ \hat{\theta} \\ \hat{\sigma} \end{bmatrix} \right)_{t=0} \quad [31]$$

Where:

B = matrix containing the decision variables (i.e., the coefficients of the piecewise polynomials that approximate the states), each column corresponding to a different state

bp = list of breakpoints, including the first and last time values of the experiment as the first and last elements, respectively

μ = list of invariable offsets for each state, used to ensure the final decision variables in B have roughly the same magnitudes across all estimates (explanation in Chapter 2.5.1)

δ = list of invariable scaling factors for each state used to ensure the final decision variables in B have roughly the same magnitudes across all estimates (explanation in Chapter 2.5.1)

Var_α, Var_ω , Var_a = known noise variances of the angular acceleration, angular velocity, and specific force measurements, respectively

j = time index, with j =1 at the first time sample in the entire experiment

n = number of time samples in the entire experiment

Hats indicate estimated measurements or states; estimated measurements are calculated from the estimated states using the Equations from Chapter 2.3

Harpoons indicate actual measurements from the sensors

Subscripts denote the names of the sensors from which the measurements came (e.g., subscript 0 refers to measurements from S_0)

Note that, assuming the sensor noises are normally distributed with zero mean, the summation terms on the right-hand side of Equation 31 are equivalent to the negative natural logarithm of the likelihood function for the estimated sensor measurements (leaving out any terms which do not depend on the estimates themselves). As a result, minimizing just the summation terms yields a maximum likelihood estimate for the ATD states (where "maximum" is with respect only to other functions of the form determined by the polynomial order and the break points). The last terms in the cost are simply the squared magnitudes of the initial estimated position, velocity, and orientation of the measurement center of S_0 in the inertial coordinate frame. The kinematic equations that relate the estimated states to the estimated sensor measurements do not have any dependence on these initial conditions, so I added these terms to the cost to prevent the estimated global pose from drifting around in the inertial reference frame. Its inclusion has no bearing on the likelihood of the resulting estimates.

To illustrate how the states and their derivatives are extracted from the arguments of F so the estimated measurements on the right-hand side of equation 31 may be

obtained, I will use the two-link kinematic chain from which Equations 1-3 in Chapter 2.3 were derived. Here, I will prescribe that link i is fixed to the inertial reference frame, so the only state in the system is λ, thus, B is a column vector and μ, δ are scalars. For convenience, I will consider a scenario with two panels, one data point per panel, and O = 3. Refer to Equations 32-35.

$$\begin{bmatrix} \mathrm{pL}_1 \\ \mathrm{pL}_2 \end{bmatrix} = \begin{bmatrix} -1 & 1 & 0 \\ 0 & -1 & 1 \end{bmatrix} bp \qquad [32]$$

$$\begin{bmatrix} \lambda_1 \\ \lambda_2 \end{bmatrix}$$

$$= \delta \underbrace{\begin{bmatrix} 1 & \frac{t_1 - bp_1}{pL_1} & \left(\frac{t_1 - bp_1}{pL_1}\right)^2 & \left(\frac{t_1 - bp_1}{pL_1}\right)^3 & 0 & 0 & 0 & 0 \\ 0 & 0 & 0 & 0 & 1 & \frac{t_2 - bp_2}{pL_2} & \left(\frac{t_2 - bp_2}{pL_2}\right)^2 & \left(\frac{t_2 - bp_2}{pL_2}\right)^3 \end{bmatrix}}_{T} B$$

$$+ \mu \begin{bmatrix} 1 \\ 1 \end{bmatrix} \qquad [33]$$

$$\begin{bmatrix} \dot{\lambda}_1 \\ \dot{\lambda}_2 \end{bmatrix} = \delta T \underbrace{\begin{bmatrix} \begin{bmatrix} 0 & 1 & 0 & 0 \\ 0 & 0 & 2 & 0 \\ 0 & 0 & 0 & 3 \\ 0 & 0 & 0 & 0 \end{bmatrix} pL_1{}^{-1} & \begin{matrix} 0 & 0 & 0 & 0 \\ 0 & 0 & 0 & 0 \\ 0 & 0 & 0 & 0 \\ 0 & 0 & 0 & 0 \end{matrix} \\ \begin{matrix} 0 & 0 & 0 & 0 \\ 0 & 0 & 0 & 0 \\ 0 & 0 & 0 & 0 \\ 0 & 0 & 0 & 0 \end{matrix} & \begin{bmatrix} 0 & 1 & 0 & 0 \\ 0 & 0 & 2 & 0 \\ 0 & 0 & 0 & 3 \\ 0 & 0 & 0 & 0 \end{bmatrix} pL_2{}^{-1} \end{bmatrix}}_{D} B \qquad [34]$$

$$\begin{bmatrix} \ddot{\lambda}_1 \\ \ddot{\lambda}_2 \end{bmatrix} = \delta T D^2 B \qquad [35]$$

Where:

t_j = time value in seconds of the j^{th} time sample

pL_i = time duration in seconds of the i^{th} panel.

Equations 32-35 can be intuitively altered for different polynomial orders, numbers of panels, and numbers of data points by altering the matrices labeled T and D. T contains the piecewise polynomial basis functions in its columns and D implements the power rule and chain rule to analytically differentiate the polynomial estimates with respect to time.

The optimization procedure is also subject to linear equality constraints that enforce continuity and twice differentiability at the break points. These are necessary to ensure the estimates are physically realizable. Again, I will use the same simple linkage as above to illustrate the structure of these constraints. Refer to equation 36.

$$\underbrace{\begin{bmatrix} 1 & 1 & 1 & 1 & -1 & 0 & 0 & 0 \\ 0 & {pL_1}^{-1} & 2{pL_1}^{-1} & 3{pL_1}^{-1} & 0 & -{pL_2}^{-1} & 0 & 0 \\ 0 & 0 & 2{pL_1}^{-2} & 6{pL_1}^{-2} & 0 & 0 & -2{pL_2}^{-2} & 0 \end{bmatrix}}_{A_{eq}} B = \begin{bmatrix} 0 \\ 0 \\ 0 \end{bmatrix} \qquad [36]$$

The first row of A_{eq} corresponds to the continuity constraint, the second to the first differentiability constraint, and the third to the second differentiability constraint. As with T and D, A_{eq} may be intuitively altered for cases with different polynomial order and number of panels, etc.

2.5.1. Generating the Initial Seed

The cost function and constraints that define the optimization are globally non-convex. Therefore, it must be seeded with an initial guess somewhere in the vicinity of the desired minimum. My algorithm accomplishes this by first using numerical

integration (Euler's method) of the IMU angular velocity measurements to generate a time series of orientation estimates for each measured segment individually. I use rotation matrixes to parameterize these orientation estimates, orthogonalizing via singular value decomposition after each time update. Using the kinematic equations, I derived the Equations 37-40 to provide a relation between numerically integrated rotation matrices and the corresponding estimates of the states. These apply for any given point in time.

$$R_{S_0} = R_x(\sigma)R_y(\theta)R_z(\varphi) \qquad [37]$$

$$R_{S_0}{}^T R_{S_1} = R_x(s)R_z(\rho) \qquad [38]$$

$$R_{S_1}{}^T R_{S_2} = R_y(f)R_x(\beta) \qquad [39]$$

$$R_{S_2}{}^T R_{S_3} = R_z(L)R_y(\epsilon) \qquad [40]$$

Where:

R_{S_i} = estimated rotation matrix for S_i (i.e., its columns estimate the coordinates of the basis vectors of the local frame of S_i in terms of the inertial reference basis)

Equation 37 can be solved for $\sigma, \theta,$ and φ directly by converting the left-hand side into its corresponding 3-2-1 Euler angle sequence. Hypothetically, Equations 38-40 could be solved similarly, and one of the resulting Euler angles would be zero. However, due numerical drift in the rotation matrices, all three angles come out non-zero in practice, and one must be simply ignored. To avoid this, I solved Equations 38-40 in a least squares sense using a Levenberg-Marquardt routine (fsolve, MATLAB, MathWorks, Natick, MA).

Solving equations 37-40 at each point in time produces estimates of the angular states of the system. To generate estimates of the linear states of the system (e.g., x, y, and z) I implemented dead reconning for the measurements from S_0 (procedure outlined in chapter 1.2). For the remainder of this thesis, I will refer to the initial estimates of all the states as the dead reckoning estimates.

The dead reckoning estimates must be approximated with piecewise polynomials so they can be fed into the main optimization as the initial seed. I did this using a quadratic programming routine subject to linear constraints of the same form shown in Equation 36 in Chapter 2.5. The cost function could have been the sum of squared error in the fits; however, this leaves room for overfitting. Of course, the break point selection method should have addressed the problem of over fitting to some degree, as it determines the model complexity based on known sensor variances. None the less, simply minimizing the squared error for each polynomial fit to the dead reckoning estimates of the states produces relatively high-curvature polynomials, which results in more work for the main optimization. I address this by including an explicit smoothing term in the quadratic cost. This term simply penalizes the sum of squares of all polynomial coefficients corresponding to bases of order greater than 2, as these terms are responsible for the time varying curvature within each panel. The smoothness of the initial seed generated by this procedure can be tuned with a scalar multiplier on the smoothing term in the cost. Due to the high degree of compression produced by approximating the data with polynomials, there are generally much fewer polynomial coefficients than there are data points, and thus, the sum of squared error in the fit easily

dominates the smoothing term unless the tuning coefficient is made relatively large. I set this tuning factor equal to the ratio of the length of the time vector to the number of polynomial panels.

Aside from smoothing the initial seed, the fitting procedure described above also centers and scales the dead reckoning estimates by their respective means and standard deviations before fitting the initial seed polynomial. The means and standard deviations of the numerically integrated states are passed to the main optimization so they can be used to properly decenter and descale the state estimates before evaluating the estimated sensor measurements in the cost function. This accounts for the terms μ and δ, introduced in Equation 31 in Chapter 2.5.

2.6. Evaluation in Simulation

I evaluated my procedure on simulated data reflecting an oblique frontal impact experiment. I modeled the ATD arm and thoracic spine assembly as a rigid body kinematic linkage in Simscape Multibody (MATLAB, MathWorks, Natick, MA). The dimensions and inertias of the ATD model do not correspond exactly to any real ATD models, but I used a Hybrid III 50th percentile male to roughly size the links. The protraction/retraction and elevation/ depression joints were given large stiffness and damping to reflect the fact that these degrees of freedom are very restricted in ATDs. The rest of the joints were just given a small damping. All joints were modeled with hard stops to limit their mobility to within anatomical ranges. To simulate an oblique frontal

impact, I subjected the thoracic spine to acceleration along the axis $\left[-\frac{\sqrt{2}}{2} \quad -\frac{\sqrt{2}}{2} \quad 0\right]$ (see Figure 2 in Chapter 2.2 for axis references). I based the magnitude of that acceleration on data measured from the impactor rod of a real pneumatic ram used in injury biomechanics testing. I tested three pulses, each with two different noise realizations, and compared the resulting estimates to the dead reckoning estimates. I sampled the experiments at 10kHz for 0.44 seconds. I set the noise standard deviations for the angular velocity measurements, angular acceleration measurements, and specific force measurements to .7 rad/s , .8 rad/s^2, and .8 m/s^2, respectively, based on background measurements collected from real impact IMUs of common use in injury biomechanics.

Chapter 3. Results

3.1. Breakpoint Selection

Figures 3-7 show exemplar intermediate results from the breakpoint selection method for the specific force measurements from S_3, the forearm IMU. These results are from one of the trials conducted with pulse number 3.

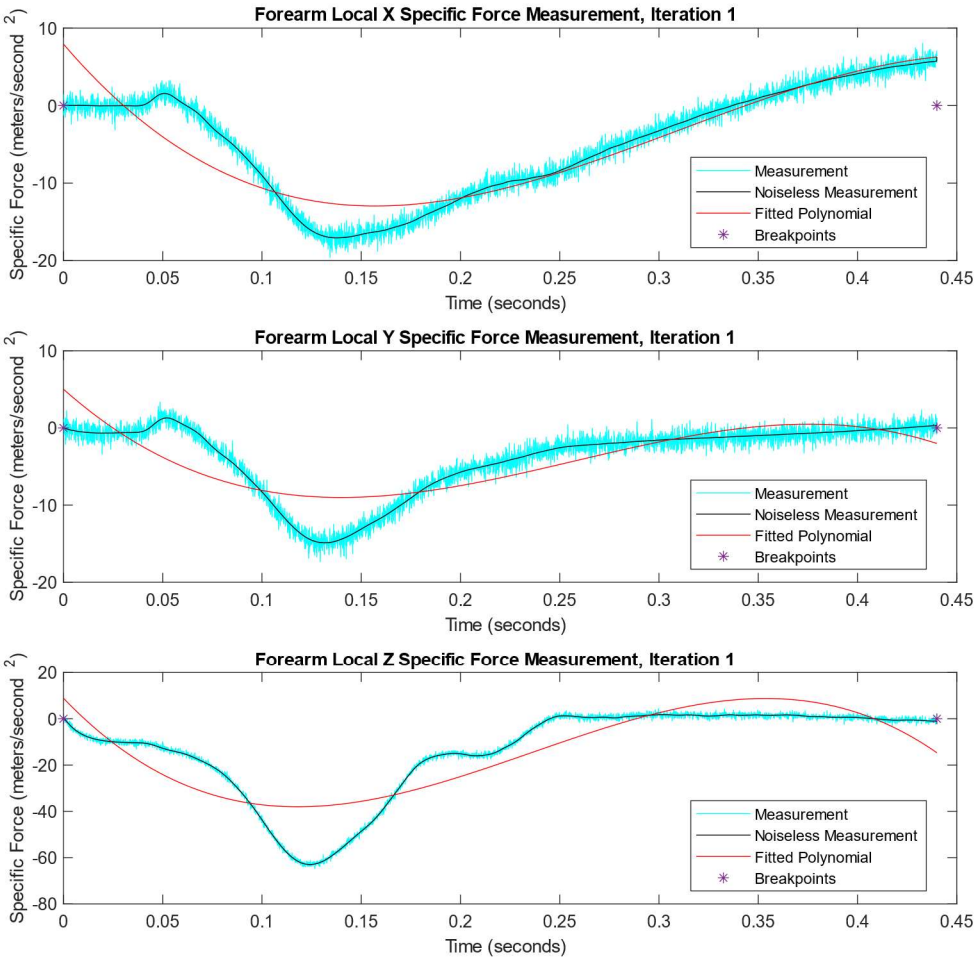

Figure 3. Exemplar First Breakpoint Selection Iteration

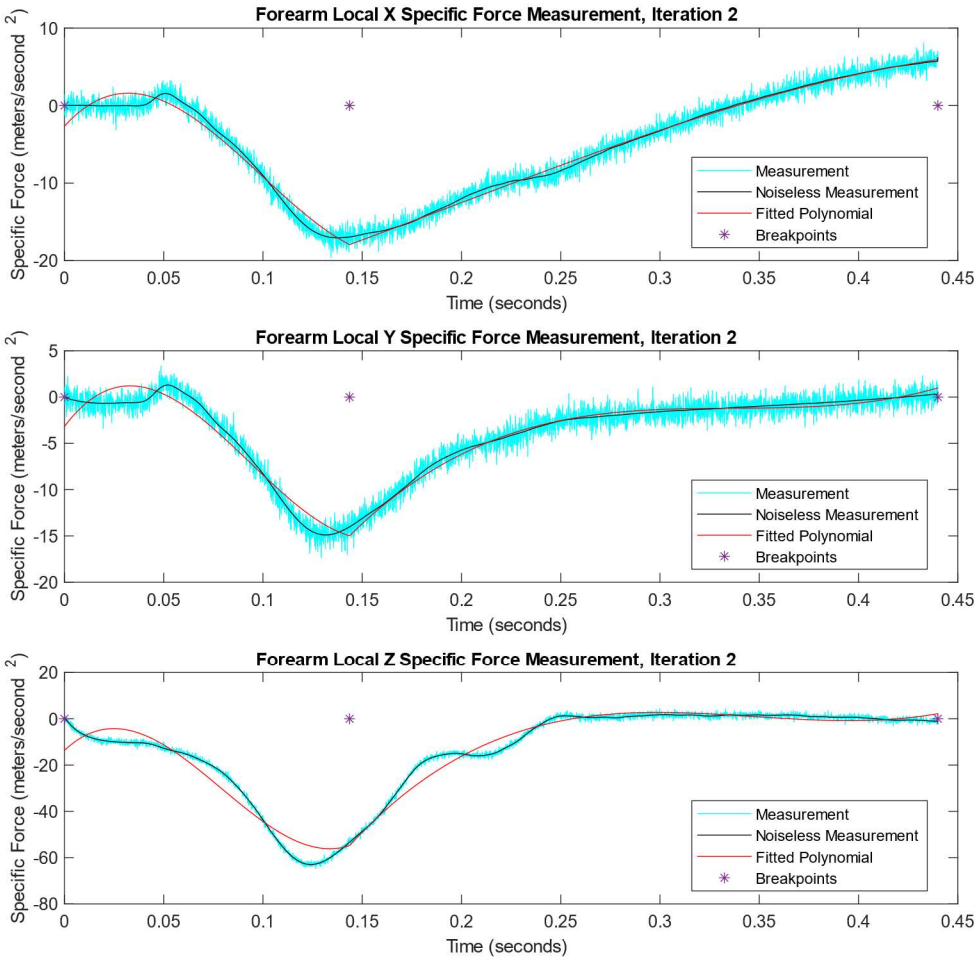

Figure 4. Exemplar Second Breakpoint Selection Iteration

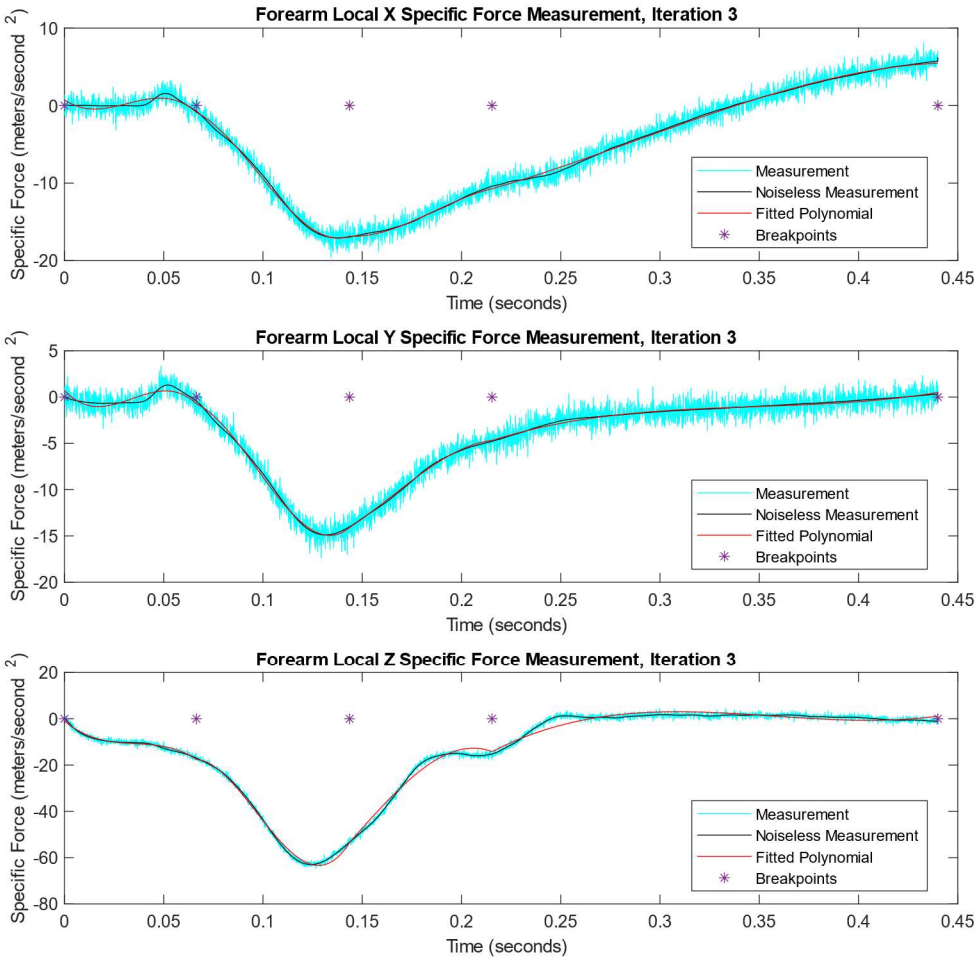

Figure 5. Exemplar Third Breakpoint Selection Iteration

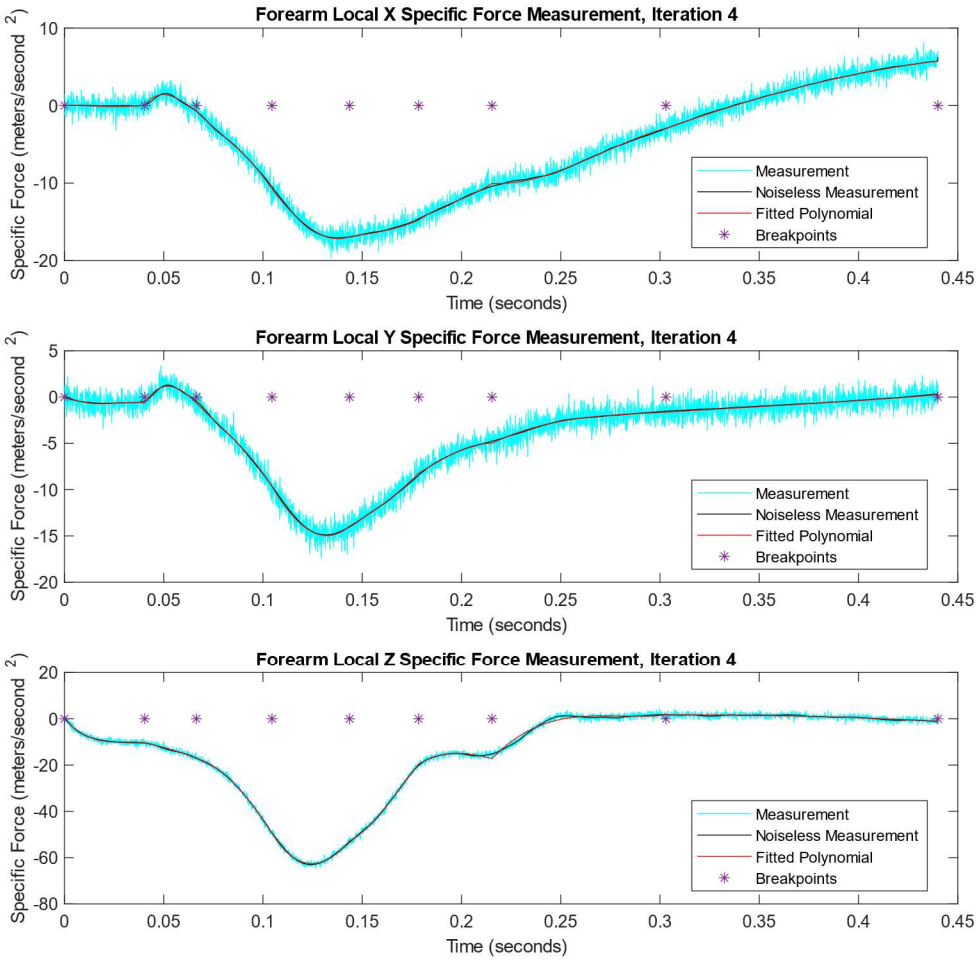

Figure 6. Exemplar Fourth Breakpoint Selection Iteration

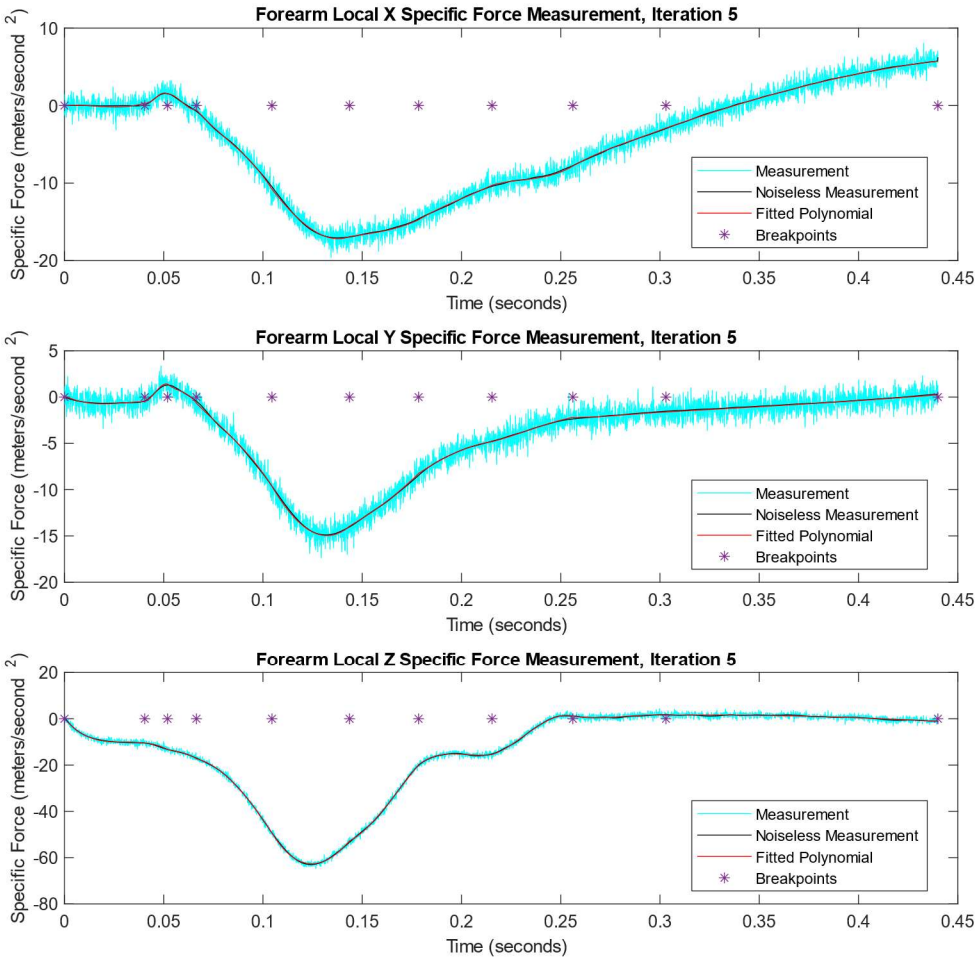

Figure 7. Exemplar Final Breakpoint Selection Iteration

3.2. Comparison of Overall Performance to Dead Reckoning

3.2.1. Example Plots from Pulse 1

Figures 8-19 show the state estimates produced by the algorithm compared against the ground truth values from the simulation and the results from dead reckoning. Figures 8-19 show the results from pulse 1. For the states pertaining to the thoracic spine link, the dead reckoning acceleration estimates are plotted because they are generated from direct measurements. For the joint angles, the dead reckoning acceleration estimates are not plotted, as they would make it difficult to see the algorithm and ground truth results because the dead reckoning joint angle accelerations require numerical differentiation.

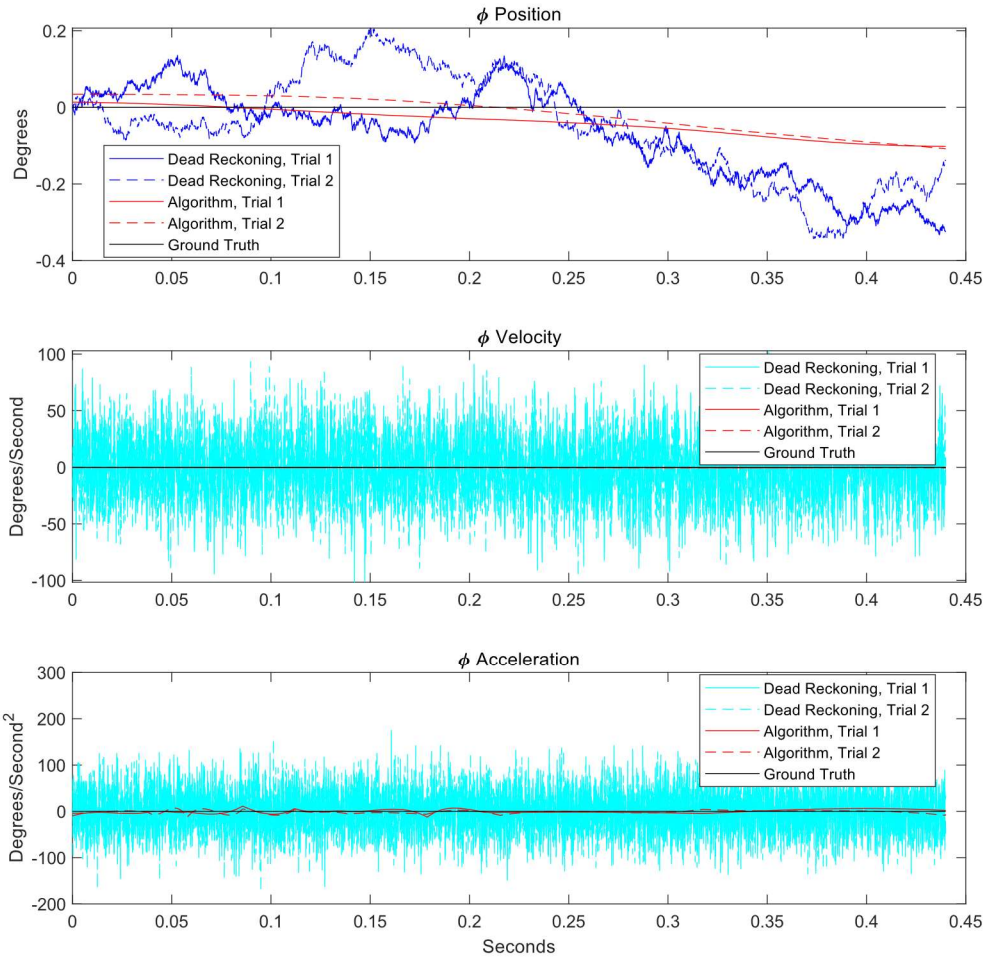

Figure 8. φ Estimates, Pulse 1

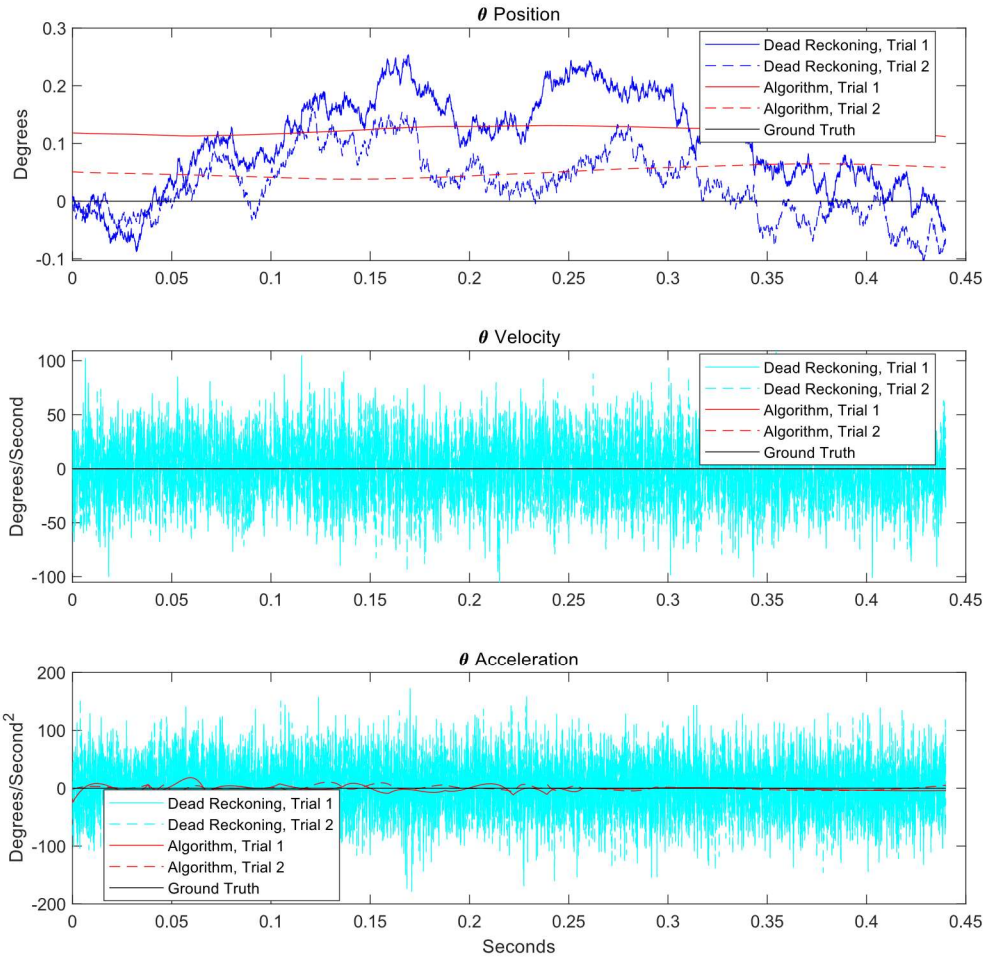

Figure 9. θ Estimates, Pulse 1

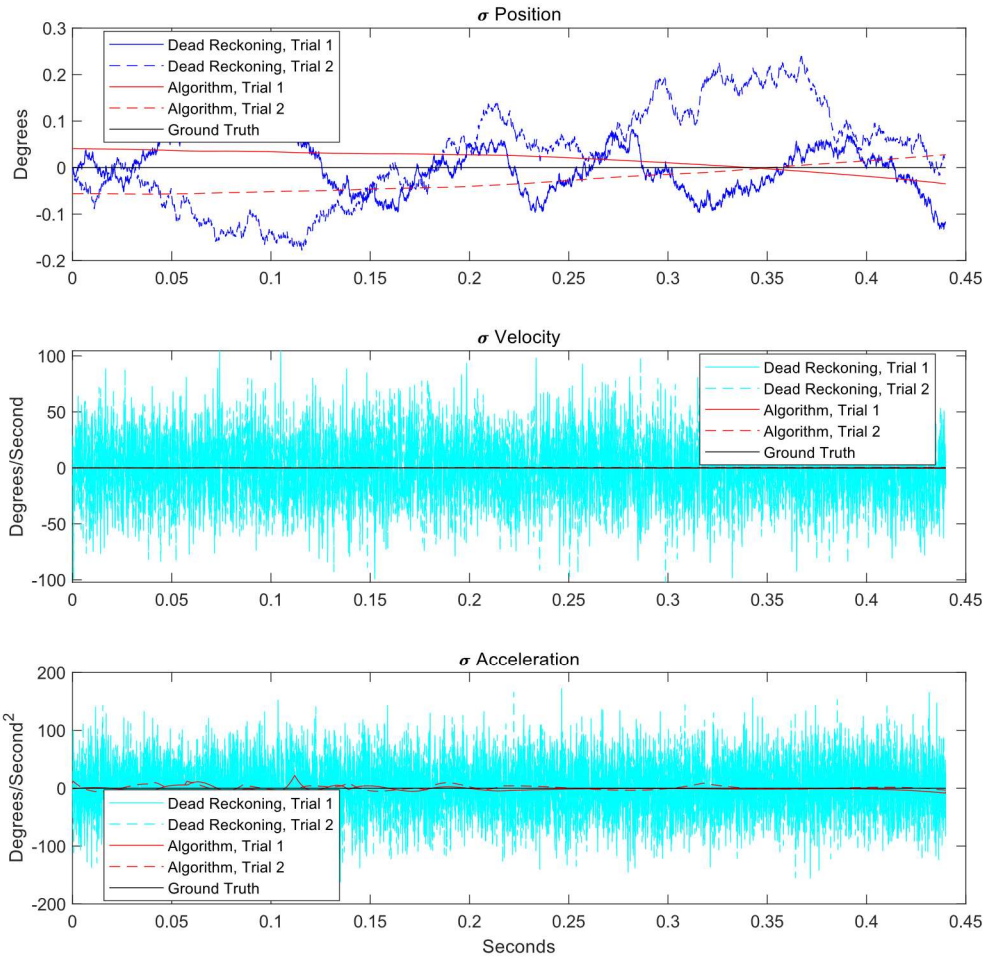

Figure 10. σ Estimates, Pulse 1

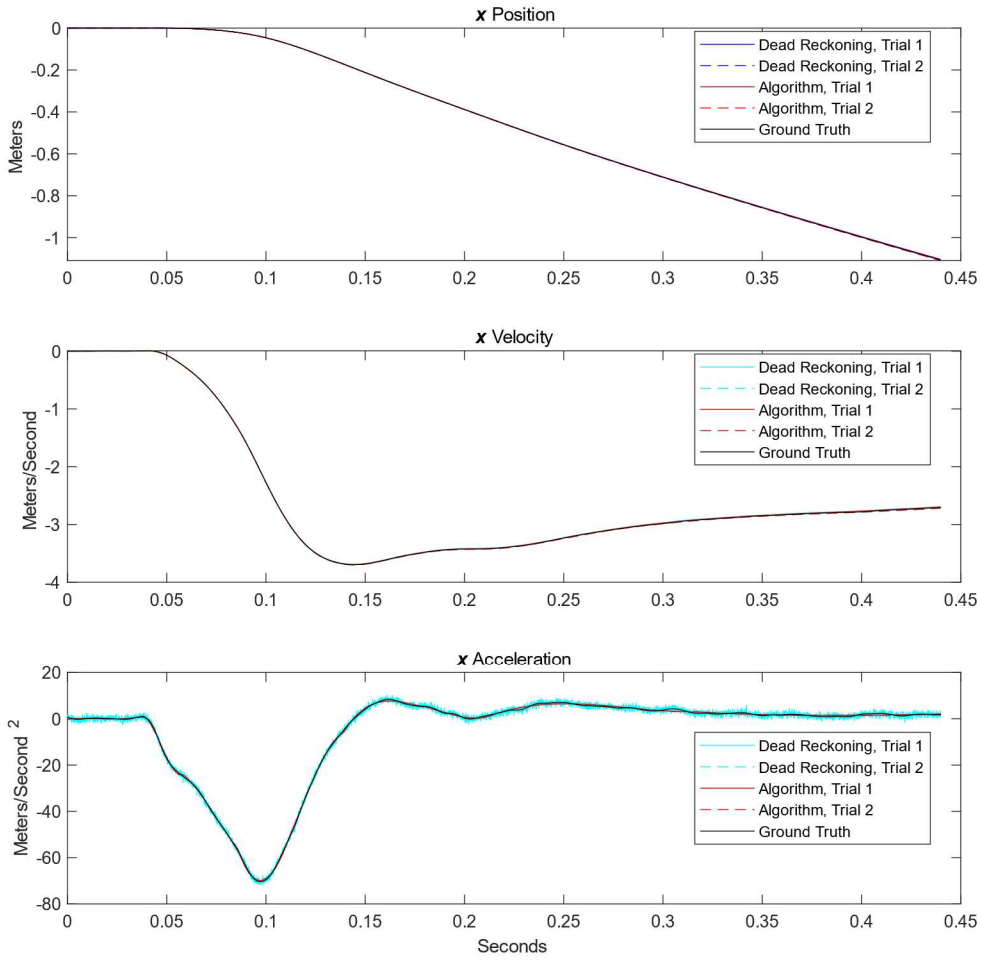

Figure 11. x Estimates, Pulse 1

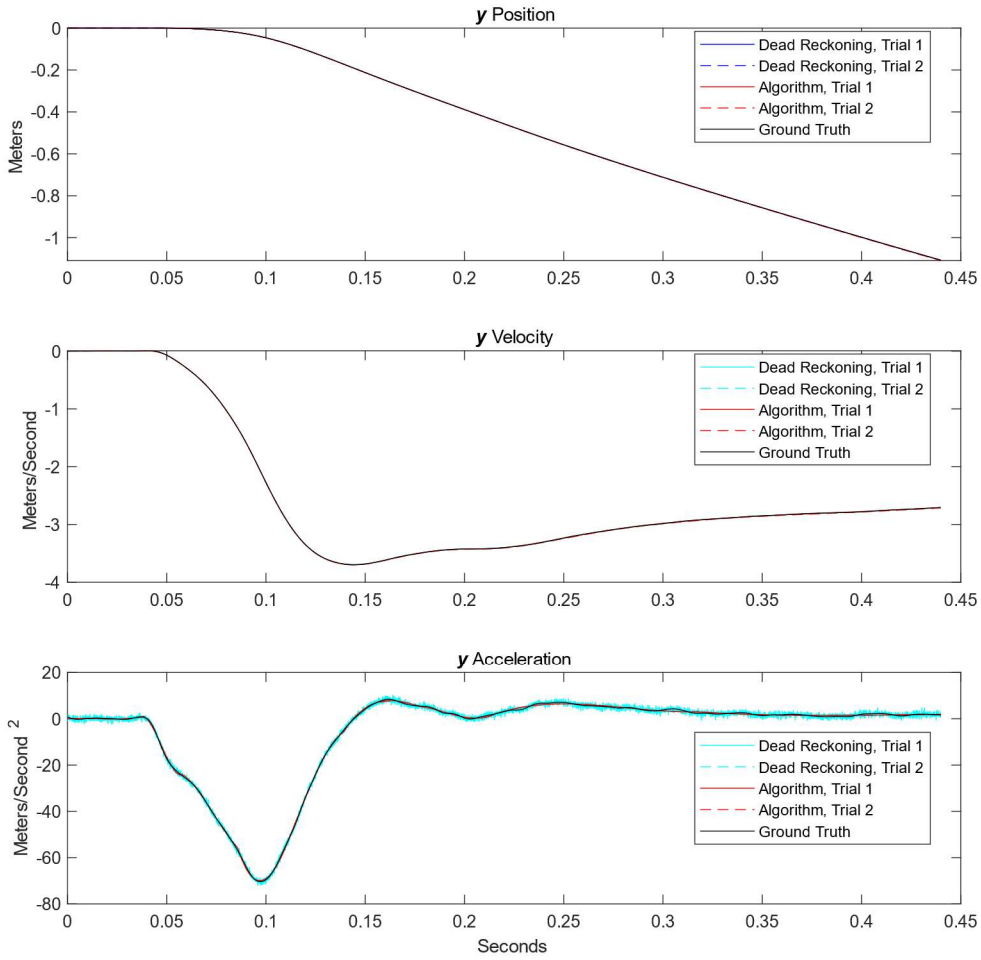

Figure 12. y Estimates, Pulse 1

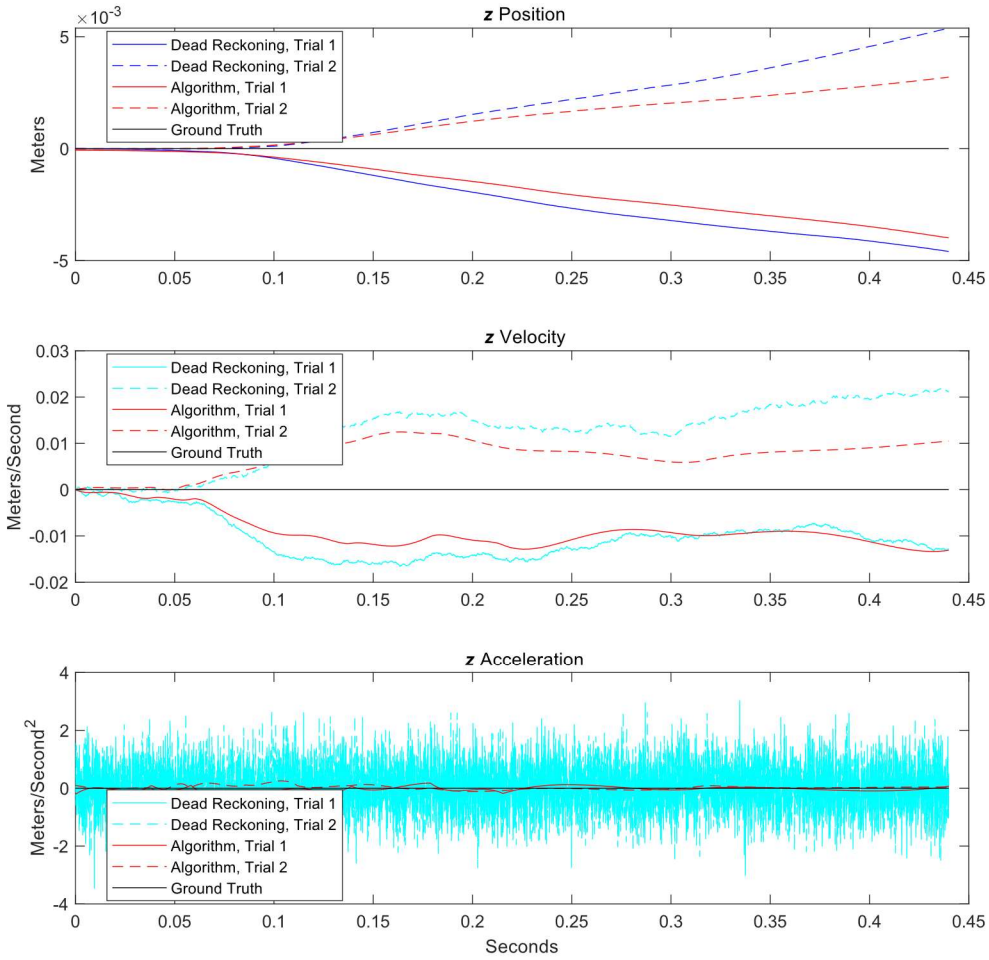

Figure 13. z Estimates, Pulse 1

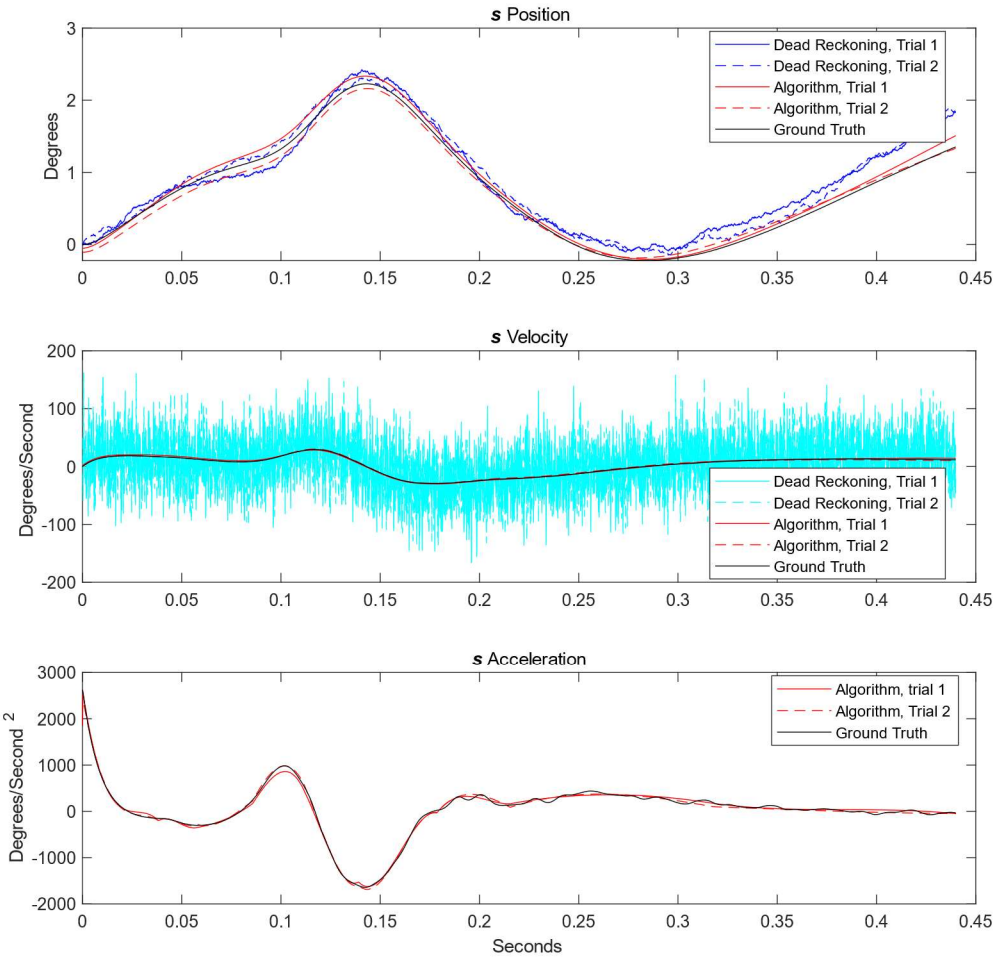

Figure 14. s Estimates, Pulse 1

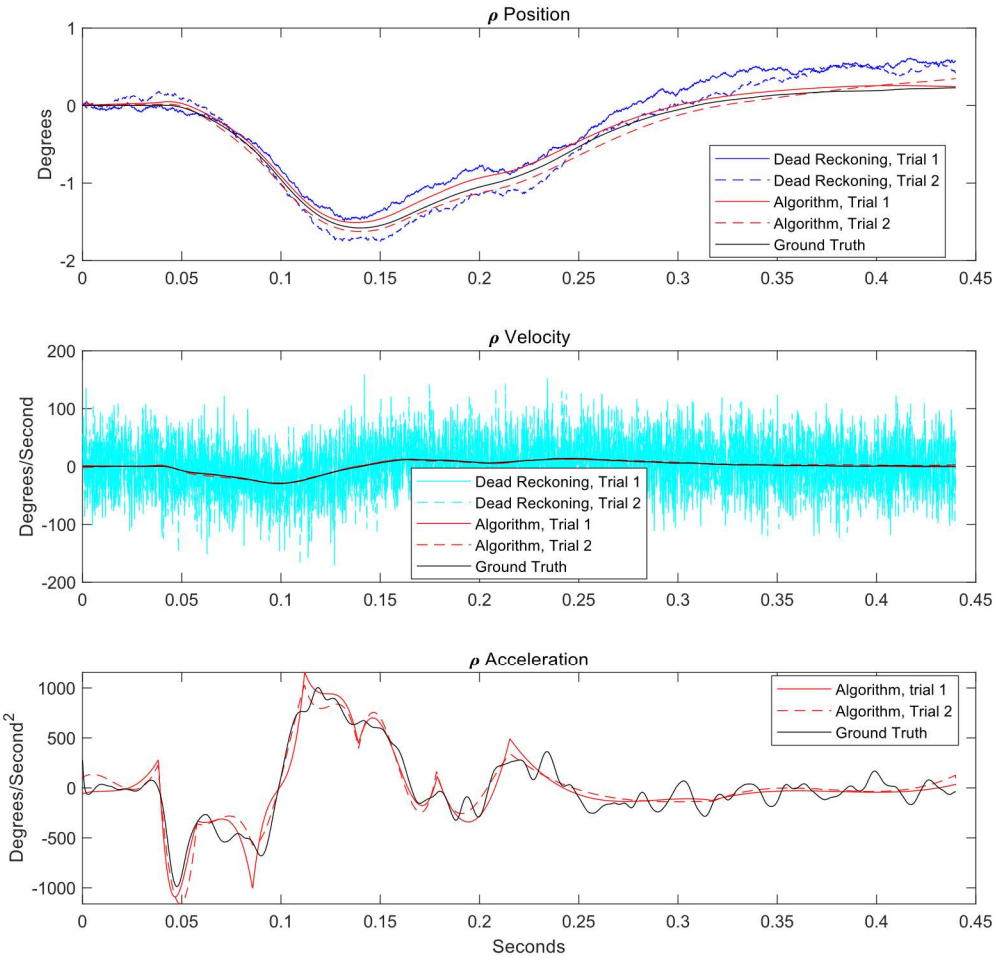

Figure 15. ρ Estimates, Pulse 1

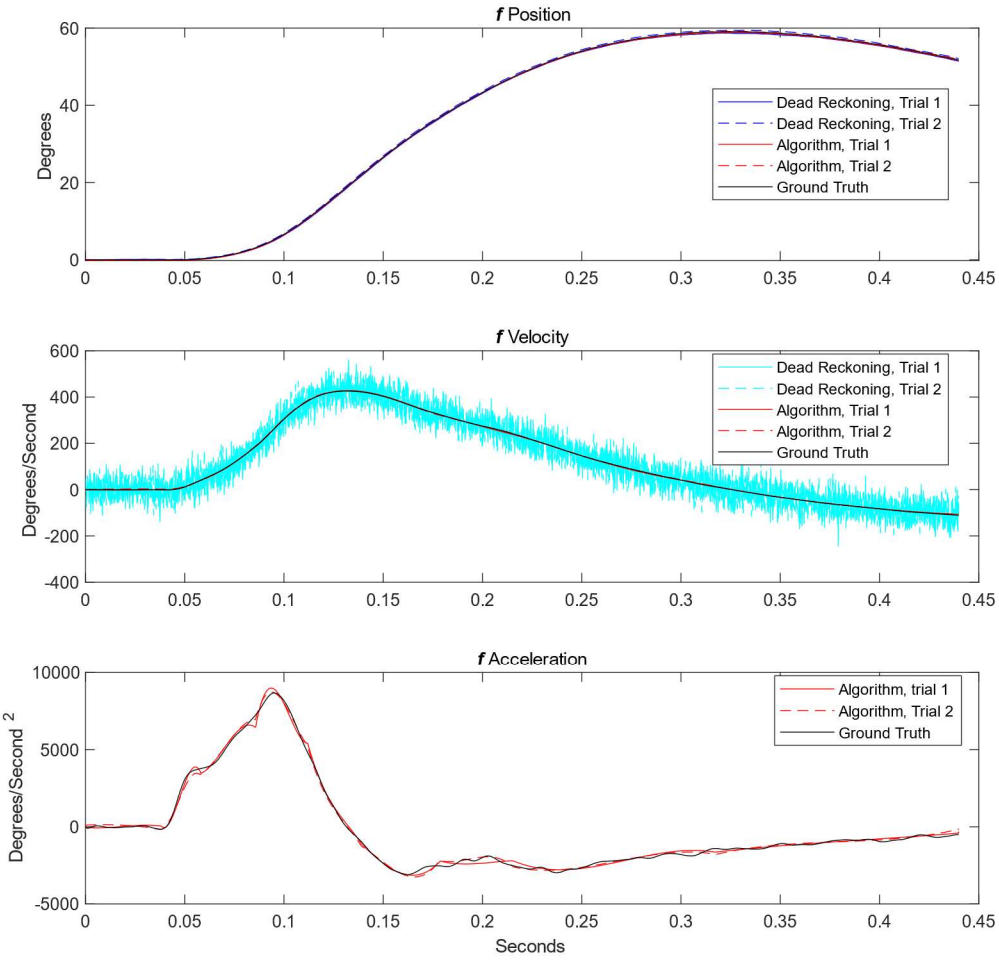

Figure 16. f Estimates, Pulse 1

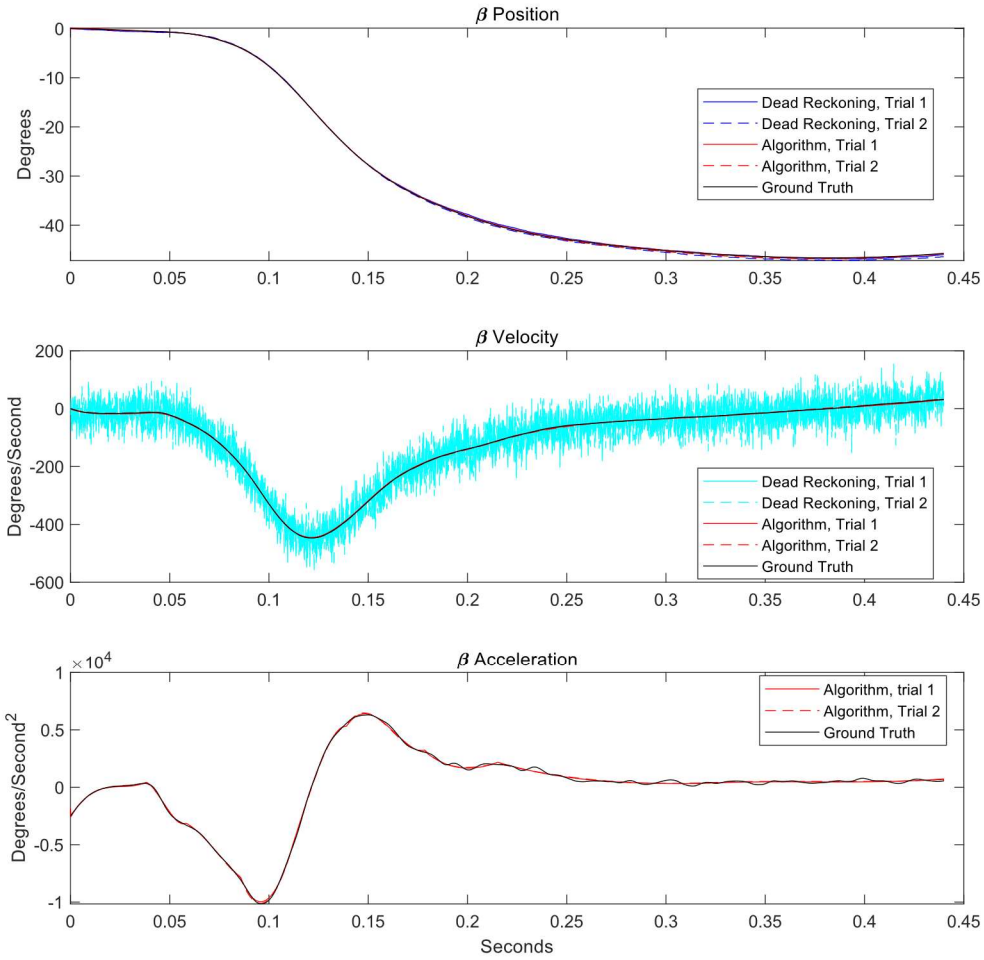

Figure 17. β Estimates, Pulse 1

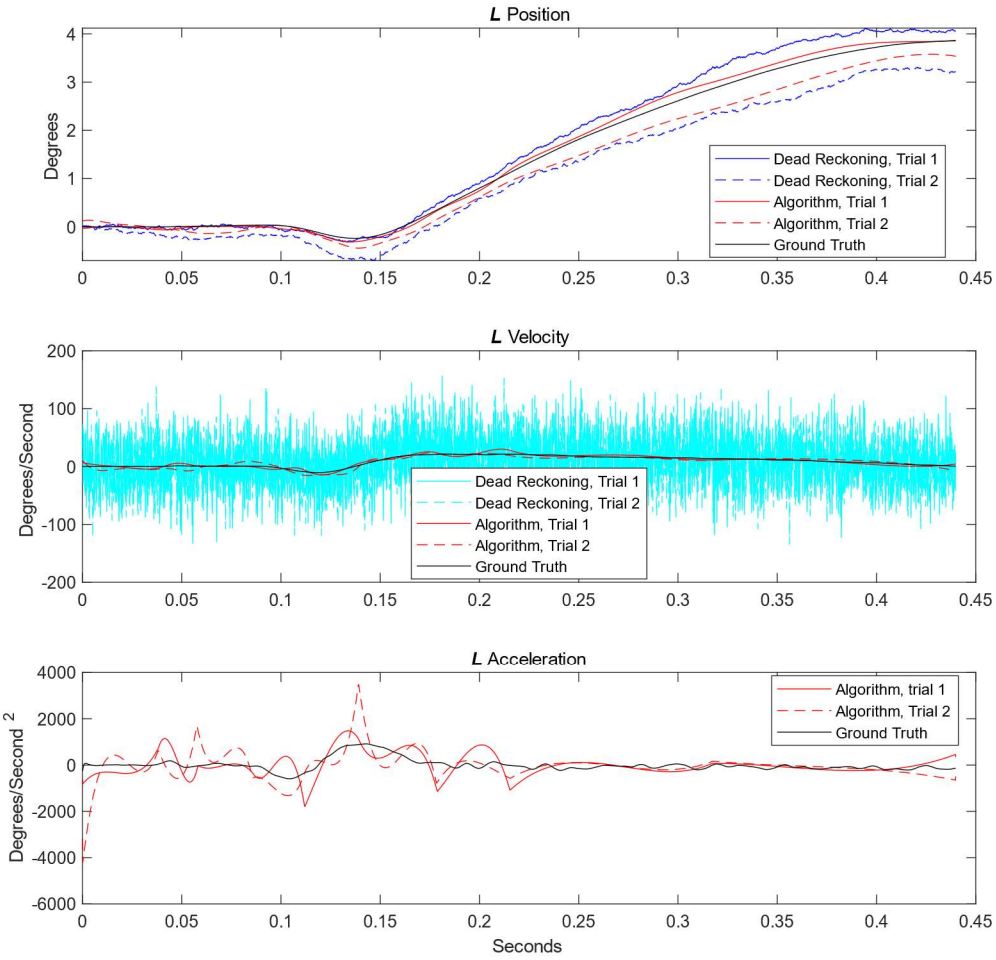

Figure 18. L Estimates, Pulse 1

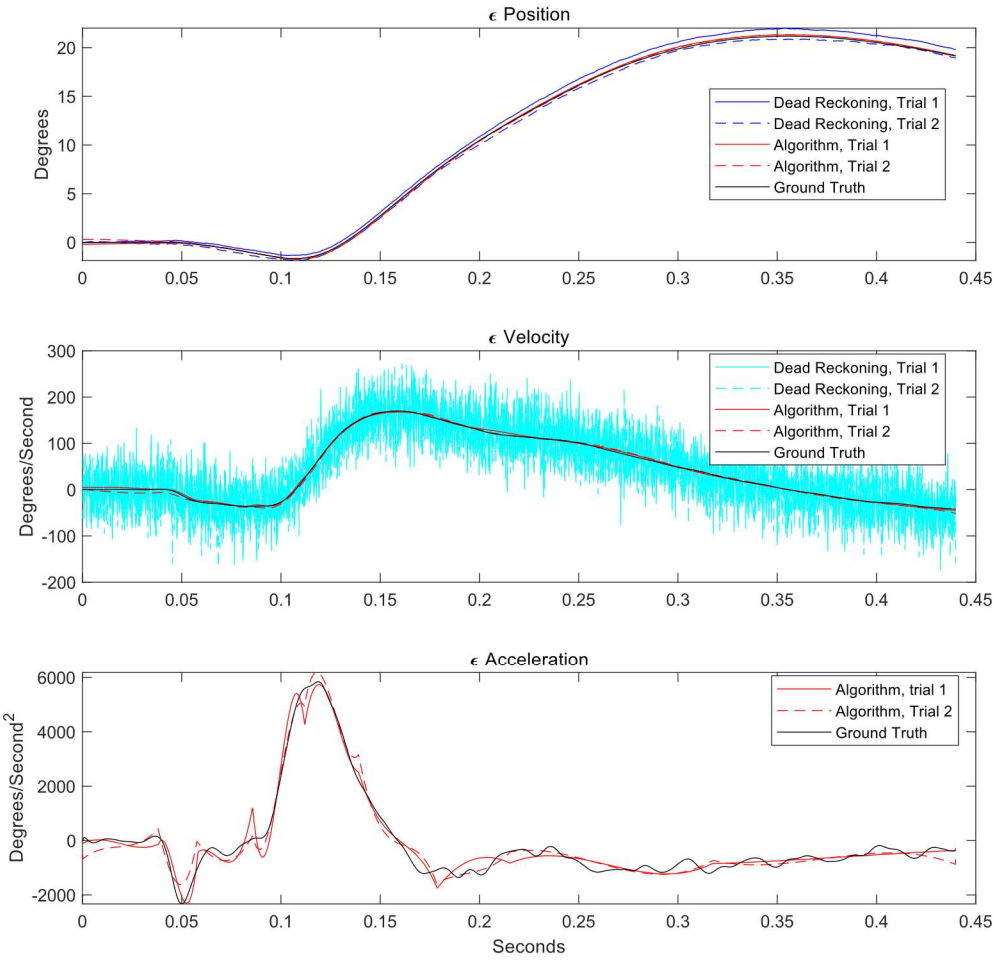

Figure 19. ϵ Estimates, Pulse 1

3.2.2. Performance Across all Trials

Figures 20-22 show the root mean squared error of the relative pose estimates (i.e., the joint angles) compared against the relative pose estimates from dead reckoning. Only the relative pose plots are shown because the algorithm has no theoretical advantage over dead reckoning for global pose. The plots show the root mean square of the error in the two estimates from the two different noise realization at each point in time. Figure 20 shows the results from pulse 1, Figure 21 shows the results from pulse 2, and Figure 22 shows the results from pulse 3.

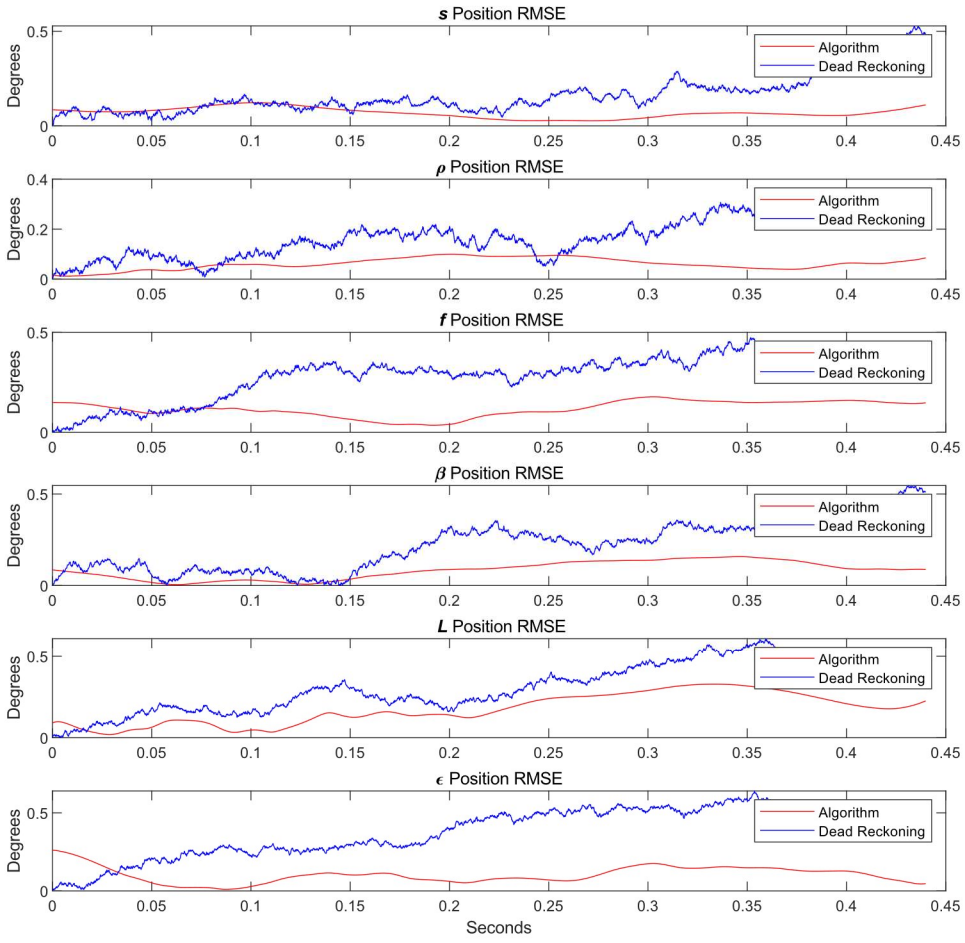

Figure 20. Root Mean Squared Error for Pulse 1 Relative Pose Estimates

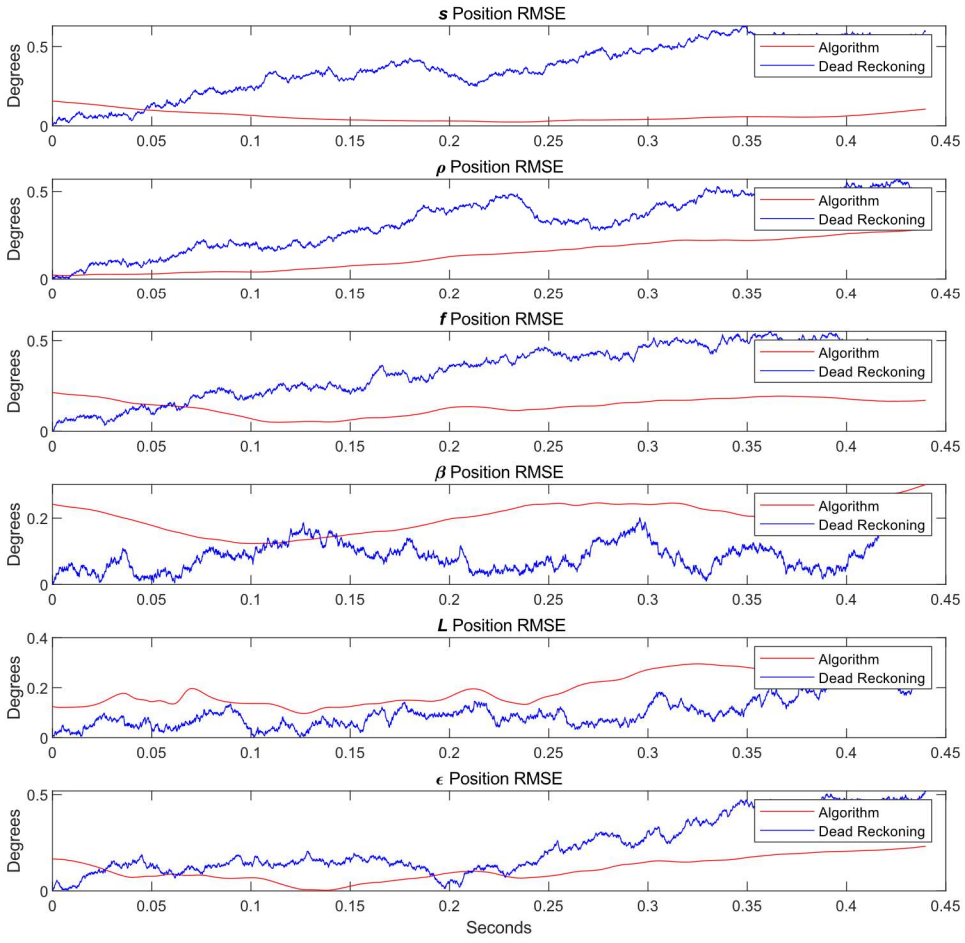

Figure 21. Root Mean Squared Error for Pulse 2 Relative Pose Estimates

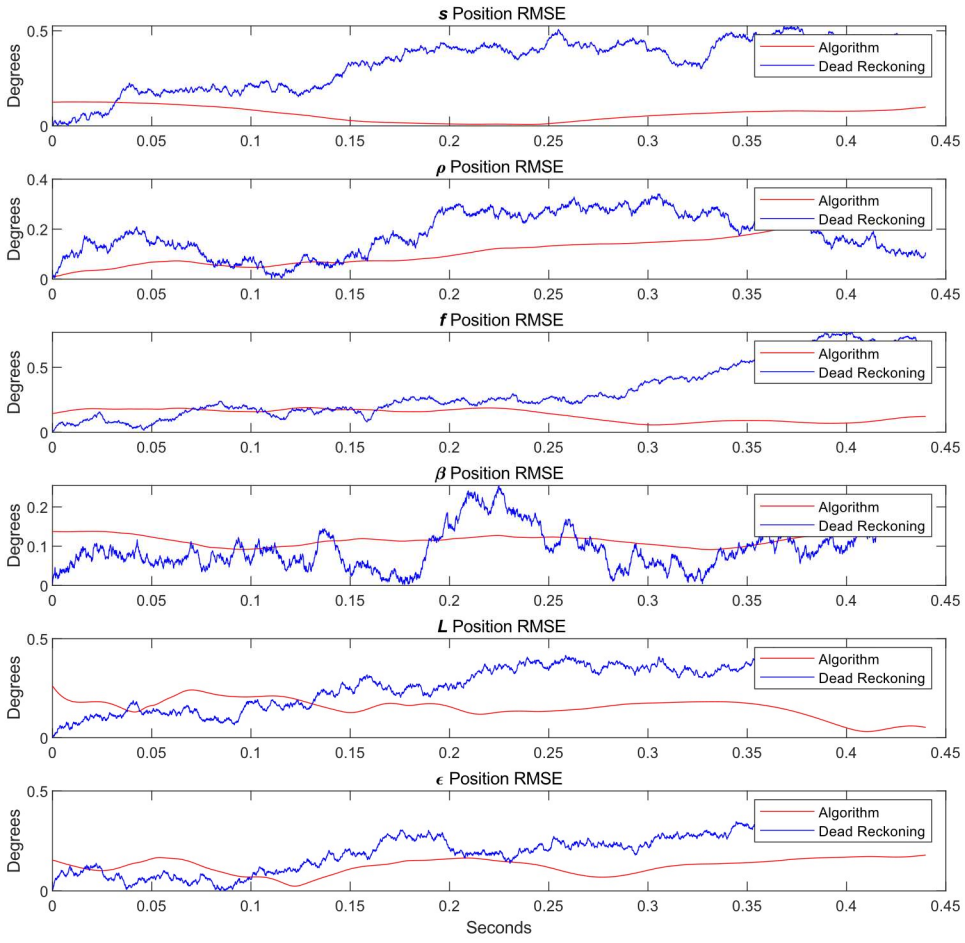

Figure 22. Root Mean Squared Error for Pulse 3 Relative Pose Estimates

The over all root mean squared errors for all estimates are listed in Tables 2 and 3. Table 2 shows the root mean squared errors for each state across the entire time interval and both noise realizations, with each pulse considered separately. Table 3 shows the overall root mean squared errors for each state taken across all trials for the entire time interval.

	Position Root Mean Squared Error (units)						Velocity Root Mean Squared Error (units/s)						Acceleration Root Mean Squared Error (units/s/s)					
	Pulse 1		Pulse 2		Pulse 3		Pulse 1		Pulse 2		Pulse 3		Pulse 1		Pulse 2		Pulse 3	
	Algorithm	Dead Reckoning	Algorithm	Dead Reckoning	Algorithm	Dead Reckoning	Algorithm	Dead Reckoning	Algorithm	Dead Reckoning	Algorithm	Dead Reckoning	Algorithm	Dead Reckoning	Algorithm	Dead Reckoning	Algorithm	Dead Reckoning
φ (degrees)	0.05	0.14	0.09	0.14	0.12	0.26	0.33	28.00	0.09	28.26	0.10	28.13	3.57	45.86	4.41	45.58	3.64	45.92
θ (degrees)	0.16	0.23	0.09	0.10	0.16	0.17	0.30	28.08	0.11	28.41	0.23	28.54	3.42	45.69	4.16	46.16	3.81	45.81
σ (degrees)	0.03	0.09	0.16	0.23	0.15	0.30	0.22	28.11	0.27	28.38	0.23	28.12	3.86	46.18	4.35	45.95	3.89	46.07
x (milimeters)	0.93	1.24	1.68	0.90	1.18	1.07	6.10	7.59	8.17	4.06	6.14	7.56	413.58	802.42	348.19	809.22	227.08	801.91
y (milimeters)	0.70	0.19	1.57	1.81	1.07	0.83	4.53	1.64	8.83	12.17	5.17	7.77	411.37	790.33	347.42	795.32	221.89	809.62
z (milimeters)	1.92	2.59	2.56	2.30	0.44	0.42	8.88	12.71	11.65	10.45	1.96	2.53	81.84	801.26	99.75	802.30	59.10	804.52
s (degrees)	0.07	0.19	0.07	0.40	0.07	0.36	1.10	40.37	0.96	40.52	0.78	39.52	44.34	285495.41	41.01	289532.45	32.52	278586.78
ρ (degrees)	0.07	0.19	0.16	0.36	0.15	0.20	1.11	39.89	1.00	39.59	1.23	40.44	116.88	284561.82	97.61	281158.41	99.78	288788.21
f (degrees)	0.12	0.30	0.15	0.37	0.14	0.38	1.62	40.58	1.35	40.40	1.80	39.94	167.85	288168.41	146.18	285873.98	149.91	282833.31
β (degrees)	0.10	0.26	0.21	0.10	0.12	0.11	1.41	40.03	1.37	39.72	0.81	40.54	121.70	281002.20	125.58	284325.49	70.45	283981.33
L (degrees)	0.20	0.35	0.21	0.12	0.16	0.30	3.31	39.51	3.33	40.08	3.10	39.91	466.30	278711.08	790.34	280244.59	794.19	281266.43
ε (degrees)	0.11	0.42	0.13	0.27	0.13	0.24	2.83	40.20	1.93	39.97	2.63	40.14	275.52	284732.57	246.11	283447.98	263.91	282603.89

Table 2. Root Mean Squared Error for Each Pulse Individually

	Position Root Mean Squared Error (units)		Velocity Root Mean Squared Error (units/s)		Acceleration Root Mean Squared Error (units/s/s)	
	Algorithm	Dead Reckoning	Algorithm	Dead Reckoning	Algorithm	Dead Reckoning
φ (degrees)	0.09	0.19	0.21	28.13	3.89	45.79
θ (degrees)	0.14	0.17	0.23	28.34	3.81	45.89
σ (degrees)	0.13	0.23	0.24	28.21	4.04	46.07
x (milimeters)	1.30	1.08	6.87	6.61	338.55	804.52
y (milimeters)	1.17	1.16	6.46	8.39	336.24	798.47
z (milimeters)	1.86	2.01	8.53	9.61	81.94	802.70
s (degrees)	0.07	0.33	0.95	40.14	39.61	284574.10
ρ (degrees)	0.13	0.26	1.12	39.97	105.11	284853.24
f (degrees)	0.14	0.35	1.60	40.31	154.94	285633.59
β (degrees)	0.15	0.17	1.23	40.10	108.85	283106.94
L (degrees)	0.19	0.27	3.25	39.83	700.67	280076.00
ε (degrees)	0.13	0.32	2.49	40.11	262.13	283596.17

Table 3. Root Mean Squared Error Across All Pulses

Chapter 4. Discussion

4.1. Instrumentation Scheme

I chose the instrumentation scheme described in this research because it represents a compromise between accuracy and practicality. Most of the available literature regarding the incorporation of kinematic constraints in the sensor fusion process for IMU measurements uses sensors placed on every single link in the chain of interest. Intuitively, a full instrumentation scheme like this provides the algorithm with more information about the kinematic state of the linkage, and thus improves the ability of the algorithm to generate accurate estimates. In the specific case of single degree of freedom revolute joints between the segments, in ensures that no numerical singularities from gimbal lock will affect the estimates. However, placing a sensor on each link of any commercially available ATD is essentially impossible without damaging the ATD skin, because the skin on the upper arm is generally mounted to the upper humerus, but it extends down to encase the lower humerus, which rotates within the cavity produced by the skin. As well, links like the humeral head simply lack the real estate to securely attach a sensor without compromising the range of motion of the adjacent joints. As result, I chose the alternating instrumentation scheme described in Chapter 2.2, which is much more physically realizable than a full placement, while still guarding against gimbal lock. However, the results show that the alternating scheme can produce issues for certain motion profiles. In the testing scenario I simulated, where the thoracic spine link was

accelerated diagonally backwards, the resulting motion of the ATD arm reliably showed small excitations in the L angle (i.e., mediolateral rotation of the lower humerus with respect to the upper humerus) and relatively small excitations in the ε angle (i.e., flexion/extension of the elbow). As a result, the forearm IMU, S_3, always had a small perpendicular distance away from the L axis. Because S_3 was the only IMU whose measurements depended on the kinematics of the L angle, this small perpendicular distance resulted in large errors in the estimations for L accelerations, as the algorithm simply multiplies the accelerations in the estimate for L by that perpendicular distance to determine the L contribution to the specific force measurements for S_3. In attempting to fit the noise in S_3, the algorithm added high magnitude noise to the acceleration estimate for L, and because the true magnitudes of the L kinematics were small, the estimates for L accelerations ended up with bad signal to noise ratios. Had the lower humerus been outfitted with an IMU, the algorithm would have been attempting to fit the accelerations in L to two different noise realizations, and thus, it would have allowed less overfitting and better estimates for the L accelerations. This was an issue in the simulations reported here, but similar issues could have arisen for different joint angles had the testing conditions been different. Despite the limitations of the alternating placement, overall, the algorithm appeared successful, and until physical experiments indicate otherwise, I consider the sensor placement scheme sufficient.

4.2. Polynomials

The breakpoint selection routine relies on an assumption that the inertial measurements corresponding to accelerations will have the same number of inflection

points as the state accelerations, and they will occur at roughly the same points in time. Referring to equations 1-3 in Chapter 2.3, it is apparent that this assumption roughly corresponds to the assumption that the joint angle accelerations will dominate the joint angle velocities. In ATD tests, where the accelerations are generally very high, but the durations over which they occur are typically very short, this is essentially guaranteed. However, the reliance on the sensor measurements forces the algorithm to generate a common set of breakpoints for all the states, as the sensor accelerations are functions of all the states simultaneously. In a scenario where the linkage being measured is self-actuating, this would be very problematic because there would be no expectation that the state accelerations should have inflections at the same times. However, for ATDs and for most other testing scenarios in injury biomechanics, the links all passively respond to a common, dominating perturbation, thus reducing the importance of different model complexities for different states.

Despite the value the polynomials provide in reducing the problem size and enabling accurate differentiation and interpolation, they are an inherent source of error in the algorithm. An example of this can be seen in the fact that the algorithm performed significantly better for accelerations in the state variable z, which was held constant, than it did for the accelerations of x and y, which varied in response to the pulse (see Tables 2 and 3 in Chapter 3.2.2). The additional error in the x and y accelerations was likely due to the limited flexibility of the polynomials.

Because the polynomials restrict the performance of the algorithm, the polynomial order and its effect on algorithm performance should be investigated

empirically, rather than being chosen arbitrarily, as I have done in this research. A crucial consideration is that the optimal choice for polynomial order likely depends on the specific test conditions, such as excitation of the states, sample rates, and sample durations, so, for the algorithm to function with comparable quality across significantly different tests, the polynomial order may require algorithmic selection, similar to the way in which the break points are currently selected based on the sensor measurements.

4.3. Theoretical Limitations

The algorithm's fundamental innovation over simple dead reckoning is the inclusion of the kinematic model. The use of polynomials provides some benefit in forcing the estimates to be locally smooth, but the kinematic model is what enables the algorithm to address integration drift, which is the main issue with dead reckoning. The inclusion of the kinematic model is fundamentally helpful in reducing drift because it provides a mechanism by which the measurements from one IMU can serve as a reference to orient the frames of other IMUs. However, this can only limit drift in the states that pertain to relative pose (i.e., the joint angles); the states pertaining to global pose are still liable to drift because the algorithm has no reference measurements for the inertial frame. This is the fundamental difficulty addressed by additional sensors such as magnetometers, as they allow the algorithm access to a vector of known orientation in the inertial frame. In the context of an ATD test, however, where magnetometers would be prone to magnetic disturbances, the tendency of the algorithm estimates for global pose to drift could be addressed by collecting measurements of the initial and final orientations of

the linkage via a digitizer, and incorporating those into the cost function, though this would likely be difficult in settings where the subject traverses a large distance, and the digitizer would need to be moved the between measurements of the initial and final pose. In sled tests, where the digitizer could be mounted to the local frame of the sled, the local pose of the ATD with respect to the sled could be accurately measured before and after the experiment, and this would practically address the issue of global pose drift, since the global orientation of the sled with respect to the inertial reference frame is generally fixed, and the global position is generally constrained to be one dimensional, and the positions at key events can be inferred from knowledge of the testing design.

The lack of advantage for global pose is apparent in the results, as the improvement achieved by the algorithm over dead reckoning for φ, θ, σ, x, y, and z were less significant than for the joint angle states, with the algorithm actually performing slightly worse than dead reconning for the x estimate on average across all pulses. The slight improvements with respect to dead reckoning seen across the other states pertaining to global pose were likely only due to the smoothness of the polynomials.

4.4. Study limitations

Though the data shows an advantage for the algorithm in estimating relative pose when compared to dead reckoning, for some states, this advantage was only apparent when results across all pulses were taken together (refer to Table 3). For β positions, the algorithm performed worse than dead reckoning on pulses 2 and 3, and for L positions, the algorithm performed worse than dead reckoning on pulse 2 (refer to Table 2). This

was likely due to two factors. The first is that the experiments were not very conducive to large drifts, given the high sample rates and absence of biases in the sensors. Indeed, the drifts observed across the board were very small. This is relevant because variations in the state positions have very little effect on the cost for estimates in the near vicinity of the truth, and thus, within that small region around the true estimate, the algorithm has very little ability to distinguish between estimates. The second is the fact that only two noise realizations were tested for each pulse. With such small sample sizes, it may be that the apparent superiority of the dead reckoning estimates for some states in some pulses is simply down to random chance. Future work should test the algorithm against dead reckoning under conditions which are more likely to produce drift, and a greater number of noise realizations should be tested for each pulse to get a better gauge of the variance of the dead reckoning estimate.

Aside from the limited ability of this work to informatively compare my algorithm to dead reckoning, it is also limited as an indicator of the applicability of my algorithm to real ATDs. Firstly, without a direct comparison to OSS measurements via physical experiment, the results presented here give no indication that the algorithm could perform as well as the current standard for pose measurement in injury biomechanics. This is especially true for this study, due to the relatively high degree of predictability ensured by the simulations. The synthetic data generated here ensured that the algorithm's kinematic model and sensor models were perfectly correct. In practice, the kinematic model will itself be an estimate generated from a collection of physical measurements taken from the ATD linkage via a digitizer, and naturally, it will be subject

to some random error. The algorithm as described here may be sensitive to these errors, and failure to account for them with a separate measurement model may result in poor estimates. Because the algorithm uses an optimization framework, incorporation of the digitizer measurement model would be relatively straight forward; just as the algorithm uses the kinematic model to calculate what the sensor measurements would be assuming the estimates of the states are perfectly correct and the sensors are noiseless, the algorithm could likewise estimate the parameters of the kinematic model and calculate what the digitizer measurements would be assuming the kinematic model is perfectly correct, and, by using a noise model for the digitizer, the relevant terms in the posterior likelihood function for the digitizer measurements could be incorporated in the cost function exactly the same way as for the sensor measurements. Essentially, this would enable the algorithm to use both the digitizer measurements and the sensor measurements to calibrate the kinematic model.

Just as the kinematic model will be an approximation based on measurements, the assumed noise distributions of the sensors will also be estimated based on data. Specifically, the noise models for the sensors will be calculated from a pre-time calibration period at the beginning of each experiment during which background noise measurements for the sensors can be collected. As a result, the parameters of their assumed distributions will be estimated from sample statistics and will therefore have standard errors. Again, the algorithm could be easily adjusted to account for this by having it estimate the parameters of the noise models, using the formulas for the standard errors to incorporate their posterior likelihood functions in the cost. This would work for

the angular acceleration and angular velocity measurements, but for the specific force measurements, their biases would need to be addressed differently. This is because, in practice, the IMUs are zeroed right before each test to remove bias, which induces predictable static biases in the specific force measurements, because they will read zero on all channels when the linkage is in its initial orientation, despite the fact they are not in free fall. Because this bias would be present in the pre-time calibration period, there would be no way to estimate the bias due to gravity from the sample statistics. However, this could be addressed by assuming the specific force measurements have two bias terms, one which is normally distributed with parameters estimated from the pre-time period, and one which is constrained to have length equal to the acceleration due to gravity.

Aside from limitations associated with uncertainties left unmodeled in the simulations, the fact that the dead reckoning estimates exhibited so little drift calls into question the robustness of the algorithm, as it relies on the dead reckoning estimate to generate the initial seed for the optimization, and the cost function is globally nonconvex. It is therefore conceivable that, under conditions where the dead reckoning estimate is worse, such as in experiments with longer durations or where sensor biases are present, the algorithm will settle into an undesirable local minimum due to a bad initial seed. Physical experiments must be conducted to assess the likelihood of this occurring under real experimental conditions.

4.5. Applicability to PMHS Testing

As discussed in chapter 1.2, the use of kinematic models in the IMU sensor fusion process has been shown in the literature to be valuable for human pose estimation in low acceleration regimes. Therefore, it is reasonable to suspect that the same may be true for PMHS testing in injury biomechanics. My algorithm provides a starting point for the development of a model based algorithm for PMHSs. The kinematic model would need to be replaced with a model for the human body as opposed to a model for an ATD, but as mentioned previously, the optimization framework makes model swapping relatively intuitive. Of course, because the human body is generally much less stiff than an ATD, a rigid body model would introduce error, however, previous research has shown rigid body models to be viable for human pose estimation, at least in low acceleration regimes. One potential difficulty that would present itself only in high acceleration regimes is the fact that the kinematic model only reflects constraints present in healthy motion. In a crash test, the subject is liable to exhibit injurious motions which necessarily violate the kinematic constraints that apply to healthy motion. At present, my research cannot answer any questions as to the practical impact these violations would have on the overall usefulness of kinematic model based sensor fusion for human pose estimation in high acceleration regimes, but future work should attempt to.

Chapter 5. Summary and Conclusions

5.1. Summary

The current standard for PMHS and ATD pose estimation is OSSs, which rely on an array of cameras and reflective markers to generate measurements of position for the markers. These systems are not entirely reliable in injury biomechanics settings, because they require extensive on site setup and calibration, and they require unobstructed lines of sight between the markers and cameras, which cannot be guaranteed in most high acceleration tests. Within the last 10 to 15 years, researchers have found that, for rigid body kinematic chains, drift free estimates of relative pose can be obtained from magnetometer free IMUs if the kinematic constraints of the linkage are exploited in the sensor fusion process. Such methods have been validated for human pose estimation in low acceleration regimes, but no work has applied kinematic constraints to IMU pose estimation within the high acceleration regimes of injury biomechanics. My work in this thesis focused on developing and validating a practical IMU instrumentation scheme and corresponding kinematic model based sensor fusion algorithm for the ATD upper limb and thoracic spine assembly as a first step in eventually reducing the necessity of OSS pose measurements in injury biomechanics. The IMU placement consists of four IMUs: one mounted to the thoracic spine, one mounted to the clavicle, one mounted to the upper

humerus, and one mounted to the forearm. The algorithm relies on all the IMUs measuring both 3D angular velocity and 3D linear specific force, while the IMU placed on the thoracic spine must also measure 3D angular acceleration. The algorithm uses an offline optimization frame work to generate continuous and twice differentiable piecewise polynomial estimates of the state positions of the ATD linkage, where the state consists of the joint angles between ATD segments and the Euler angles and cartesian coordinates of the ATD thoracic spine with respect to the inertial reference frame. The objective function for the optimization uses the kinematic model of the linkage to calculate what the sensor measurements would be, assuming a given set of estimates is perfectly correct and the sensors are noiseless. It uses these estimated sensor measurements along with zero mean gaussian noise models for the sensors to evaluate the negative natural logarithm of the posterior likelihood function for the observed sensor measurements, which the optimization routine seeks to minimize, thus the optimization seeks to maximize the likelihood of the estimates. The polynomials are used as a method of data compression to reduce the computational expenditure of the optimization procedure, and they also enable accurate differentiation and interpolation of the resulting estimates. The break points for the polynomials are spaced via a novel iterative method that uses the sensor noise models to avoid overfitting while still ensuring enough model flexibility to capture meaningful variance. The initial seed for the optimization is generated by fitting regression splines with smoothing to the estimates that result from simple dead reckoning.

The algorithm was tested in simulation with a perfectly known kinematic model and zero mean gaussian sensor noise with perfectly known noise variances. The algorithm estimates were compared to dead reckoning, and the results show (somewhat inconclusively, due to small sample sizes and unrealistically good dead reckoning estimates) that the algorithm outperforms dead reckoning across all joint angle estimates, and it performs similarly to dead reckoning on estimates corresponding to the pose of the thoracic spine with respect to the inertial reference frame. The data also shows that the polynomials, though useful, inherently limit the performance of the algorithm, and that the alternating sensor placement (as opposed to full placement with IMUs on every segment) can disadvantage some estimates with respect to others, depending on the specific motion profile observed in the test.

5.2. Conclusions and Future work

Though the algorithm performed promisingly in simulation, this research is limited in its ability to make conclusive statements about the viability of this algorithm in the real world. Future work must conduct physical experiments which compare the algorithm estimate to direct pose measurements from OSSs to make any valid conclusions. Because the simulations allowed the algorithm access to a perfect kinematic model and perfect noise models, the physical experiments may very well show the current algorithm to be insufficient for the real world. However, the use of an optimization framework allows additional uncertainties likely to be present in physical experiments (e.g., sensor biases, uncertain noise variances, and uncertainty in the kinematic model stemming from digitization error) to be intuitively incorporated into the

objective function in the event physical experiments show that additional considerations are necessary. A fundamental limitation of the algorithm, no matter how many additional sources of uncertainty are considered, is that it can only provide an advantage for drift in the states corresponding to the relative pose of the ATD links in some local frame (i.e., the joint angles). For global pose estimates (i.e., the pose of the thoracic spine link with respect to the inertial reference frame), the algorithm is liable to drift, and its only advantages over dead reckoning for these states stem from the local smoothness of the polynomial estimates. This issue may be addressed with the inclusion of digitization measurements to evaluate the initial and final pose of the linkage, which could then be intuitively considered in the objective function in the same manner as the IMU measurements.

Bibliography

[1] Tannous, Rabih & Eppinger, Rolf & Sun, Emily & Bandak, Faris & Haffner, Mark & Khaewpong, Nopporn & Maltese, Matt & Kuppa, Shashi & Nguyen, Thuvan & Takhounts, Erik & Zhang, Anna & Saul, Roger. (1999). Development of Improved Injury Criteria for the Assessment of Advanced Automotive Restraint Systems - II. National Highway Traffic Safety Administration

[2] Ash, J.H., Lessley, D., Forman, J., Zhang, Q., Shaw, C.G., & Crandall, J.R. (2012). Whole-Body Kinematics: Response Corridors for Restrained PMHS in Frontal Impacts. International Research Council on Biomechanics of Injury

[3] Eline van der Kruk & Marco M. Reijne (2018) Accuracy of human motion capture systems for sport applications; state-of-the-art review, European Journal of Sport Science, 18:6, 806-819, DOI: 10.1080/17461391.2018.1463397

[4] Kang YS, Moorhouse K, Bolte JH. Measurement of six degrees of freedom head kinematics in impact conditions employing six accelerometers and three angular rate sensors (6aω configuration). J Biomech Eng. 2011 Nov;133(11):111007. DOI: 10.1115/1.4005427. PMID: 22168739.

[5] M. Kok, J. D. Hol, and T. B. Sch¨on. Using inertial sensors for position and orientation estimation. Foundations and Trends on Signal Processing, 11(1–2):1–153, 2017.

[6] Glen Cooper, Ian Sheret, Louise McMillian, Konstantinos Siliverdis, Ning Sha, Diana Hodgins, Laurence Kenney, and David Howard. Inertial sensor-based knee

flexion/extension angle estimation. Journal of Biomechanics, 42(16):2678–2685, December 2009. ISSN 0021-9290. doi: 10.1016/j. jbiomech.2009.08.004.

[7] D. Laidig, T. Schauer, and T. Seel. Exploiting kinematic constraints to compensate magnetic disturbances when calculating joint angles of approximate hinge joints from orientation estimates of inertial sensors. In Proceedings of the International Conference on Rehabilitation Robotics (ICORR), pages 971–976, London, UK, July 2017.

[8] Thomas Seel, Thomas Schauer, and J¨org Raisch. Joint axis and position estimation from inertial measurement data by exploiting kinematic constraints. In Proceedings of the IEEE International Conference on Control Applications, pages 45–49, Dubrovnik, Croatia, October 2012.

[9] Fredrik Olsson, Manon Kok, Thomas Seel, and Kjartan Halvorsen. Robust plug-and-play joint axis estimation using inertial sensors. MDPI Sensors, 20(12):3534, 2020.

[10] D. Laidig, D. Lehmann, M. A. B´egin, and T. Seel. Magnetometer-free realtime inertial motion tracking by exploitation of kinematic constraints in 2-DOF joints. In Proceedings of the 41st IEEE International Engineering in Medicine and Biology Conference (EMBC), Berlin, Germany, July 2019.

[11] H. J. Luinge, P. H. Veltink, and C. T. M. Baten. Ambulatory measurement of arm orientation. Journal of Biomechanics, 40(1):78–85, January 2007. ISSN 0021-9290, 1873-2380. doi: 10.1016/j. jbiomech.2005.11.011.

[12] D. Laidig, P. Mueller, and T. Seel. Automatic anatomical calibration for IMU-based elbow angle measurement in disturbed magnetic fields. Current Directions in Biomedical Engineering, 3(2): 167–170, 2017. ISSN 2364-5504. doi: 10.1515/cdbme-2017-0035.

[13] D. Lehmann, D. Laidig, R. Deimel, and T. Seel. Magnetometer-free inertial motion tracking of arbitrary joints with range-of-motion constraints. In Proceedings of the 21st World Congress of the International Federation of Automatic Control (IFAC), pages 1–8, Berlin, Germany, July 2020.

[14] M. Kok, J. D. Hol, and T. B. Sch¨on. An optimization-based approach to human body motion capture using inertial sensors. In Proceedings of the 19th World Congress of the International Federation of Automatic Control (IFAC), pages 79–85, Cape Town, South Africa, August 2014.

[15] J. D. Hol. Sensor fusion and calibration of inertial sensors, vision, ultra-wideband and GPS. Dissertation no. 1368, Link¨oping University, Link¨oping, Sweden, June 2011.

[16] M. Miezal, B. Taetz, and G. Bleser. On inertial body tracking in the presence of model calibration errors. MDPI Sensors, 16(7):1132, 2016.

[17] I. Weygers, M. Kok, H. de Vroey, T. Verbeerst, M. Versteyhe, H. Hallez, and K. Claeys. Drift-free inertial sensor-based joint kinematics for long-term arbitrary movements. IEEE Sensors Journal, 20(14):7969–7979, 2020.

[18] J. K. Lee and T. H. Jeon. Magnetic condition-independent 3D joint angle estimation using inertial sensors and kinematic constraints. MDPI Sensors, 19(24):5522, 2019.

[19] B. Fasel, J. Sp¨orri, J. Chardonnens, J. Kr¨oll, E. M¨uller, and K. Aminian. Joint inertial sensor orientation drift reduction for highly dynamic movements. IEEE Journal of Biomedical and Health Informatics, 22(1):77–86, 2018.

[20] Eva Dorschky, Marlies Nitschke, Ann-Kristin Seifer, Antonie J. van den Bogert, and Bjoern M. Eskofier. Estimation of gait kinematics and kinetics from inertial sensor data

using optimal control of musculoskeletal models. Journal of Biomechanics, 95:109278, 2019.

[21] K. Eckhoff, M. Kok, S. Lucia, and T. Seel. Sparse magnetometer-free inertial motion tracking–a condition for observability in double hinge joint systems. In Proceedings of the 21st World Congress of the International Federation of Automatic Control (IFAC), pages 1–8, Berlin, Germany, 2020.

[22] Kok, M., Eckhoff, K., Weygers, I., & Seel, T. (2021). Observability of the relative motion from inertial data in kinematic chains. ArXiv, abs/2102.02675.